TELESEISMIC IMAGING: FIELD STUDY IN SOUTHERN ALBERTA AND NUMERICAL SIMULATIONS OF INVERSE SCATTERING

by

JEFFREY CHILVER SHRAGGE

BSc.(Hons), Queen's University, 1998

A THESIS SUBMITTED IN PARTIAL FULFILLMENT OF

THE REQUIREMENTS FOR THE DEGREE OF

MASTER OF SCIENCE

in

THE FACULTY OF GRADUATE STUDIES

(Department of Earth and Ocean Sciences)

We accept this thesis as conforming

to the required standard

THE UNIVERSITY OF BRITISH COLUMBIA

February 2001

In presenting this thesis in partial fulfilment of the requirements for an advanced degree at the University of British Columbia, I agree that the Library shall make it freely available for reference and study. I further agree that permission for extensive copying for scholarly purposes may be granted by the head of my department or by his or her representatives. It is understood that copying or publication of this thesis for financial gain shall not be allowed without my written permission.

Department of Earth and Ocean Sciences

The University of British Columbia

2219 Main Mall

Vancouver, BC, Canada

V6T 1Z4

Date:

15/02/2001

Abstract

This thesis consists of two parts. Part I presents results from a LITHOPROBE teleseismic experiment undertaken across southern Alberta. Relative *P*-wave delay-times from 293 earthquakes have been inverted for upper mantle velocity perturbations. The recovered model reveals a high velocity anomaly underlying a substantial portion of the southern Hearne Province to depths of 200-250 km which is interpreted as the signature of deep-seated lithospheric structure. This result suggests that, contrary to recent tectonic models, the bulk of the lithosphere in this region has remained essentially intact. In particular, it appears unlikely that evidence for extensive lower crustal melting is due to wide-scale lithospheric delamination. However, observed high mantle conductivity may be the result of small volumes of connected hydrous minerals or some other conductive species introduced during subduction that contributed to the construction of a root. Multi-event *SKS*-splitting results yield an average delay-time of 0.82 ± 0.30 s and fast polarization direction of $45° \pm 8°$ which broadly coincides with both the presumed orientation of fossil strain fields related to the ca. 1.8 Ga NW-SE shortening of the Hearne Province and absolute North America plate motion. Processing of receiver functions yields Moho depth estimates which are fairly uniform ($\sim$38 km) beneath northern stations, but show crustal thickening ($>$40 km) within the Medicine Hat Block.

Part II investigates the formal inversion of synthetic teleseismic *P*-coda waves for subsurface elastic properties using an asymptotic method which assumes single-scattering. The model comprises an idealized lithospheric suture zone. Two dimensional, pseudo-spectral synthetic seismograms representing a plane *P*-wave incident upon this structure are preprocessed to extract an estimate of the scattered wavefield. These data are employed in a series of experiments that examine the dependence of multi-parameter inversion on a range of input parameters and demonstrate: i) the contrasting sensitivity which forward- and back-scattered waves display to structural recovery; ii) the diminution of the problem null-space accompanied by increased source coverage; iii) improvements in model reconstruction achieved through simultaneous treatment of multiple scattering modes; and iv) the robustness of the approach for data sets with noise levels and receiver geometries that approach those of field experiments.

Table of Contents

List of Tables

List of Figures

Acknowledgements

A big thank you my supervisor Michael Bostock for his seemingly endless patience and mentorship during those early days of seismology and writing. Thanks also to the earthquake seismology group, Charly Bank, Andy Frederiksen and Stéphane Rondenay for a wonderfully stimulating environment that enriched my daily routine. Thanks to the my co-supervisor Bob Ellis and Ron Clowes, for providing insightful and constructive input at various stages during the progress of this research. This research was supported financially by NSERC grants to Michael Bostock and Bob Ellis.

For Baboo

Chapter 1

Motivation for Thesis

The structure and dynamics of the Earth's lithosphere have a significant impact upon human society by virtue of our reliance on natural resources, and the substantial devastation that is regularly wrought by earthquakes and volcanic activity. These two factors provide much of the impetus for the use of geophysics in understanding shallow crustal structure and processes. However, geophysics, and seismology in particular, are also used in more fundamental studies to characterize deeper portions of the lithosphere and upper mantle. In both fundamental and applied contexts there is a continual drive to develop novel approaches to processing that afford improved resolution for challenging structural targets.

In Canada, LITHOPROBE studies, spearheaded by the seismic reflection method, have assembled much detailed information concerning lithospheric structure and evolution across the Canadian landmass. It is worth noting, however, that a majority of the lithospheric plate resides below the crust-mantle boundary and, due to the stronger rheology of mantle materials, it may exert a substantial influence on the near-surface evolution. The use of seismic reflection methods in characterizing the lithospheric mantle is hindered by the limited depth penetration and frequency bandwidth of anthropogenic sources. In contrast, teleseismic waves (seismic waves generated by earthquakes at epicentral distances $> 30°$) do not suffer from these shortcomings to the same degree and allow a more comprehensive characterization of sub-crustal lithospheric structures.

This thesis investigates two different aspects of the use of teleseismic analysis techniques in

the recovery of lithospheric structure. In Part I, the application of travel-time tomography, shear wave splitting, and radial receiver functions to a suite of teleseismic seismograms recorded in the Hearne Province of southern Alberta is described. Geophysical constraints resulting from these analyses are subsequently interpreted to shed light on the tectonic evolution of a region which is hidden from view by the thick sequences of the Western Canada Sedimentary Basin. As such, the work documented in Part I of this thesis presents a passive-source study of the upper mantle of Alberta at a length-scale comparable to or exceeding large-scale refraction profiling (e.g., DEEP PROBE), and stands as an important contribution to the understanding of the assembly of the Laurentia supercontinent.

Part II of this thesis investigates a new high-resolution teleseismic imaging technique that draws motivation from the increasing availability of broadband, three-component instruments and the seismic migration problem in hydrocarbon exploration. This method provides a rigorous basis for the inversion of teleseismic wavefields recorded on dense receiver arrays for Earth's elastic parameters. I discuss the implementation of this new technique on a set of synthetic data with the objective of assessing the potential and limitations of the inversion methodology in recovering discontinuous model structure. In particular, this work identifies the roles that various parameters play in the inversion process, and demonstrates the feasibility of the approach prior to its application to field data.

Part I

INTEGRATED TELESEISMIC STUDIES OF THE SOUTHERN ALBERTA UPPER MANTLE

Chapter 2

Introduction and Study Area Overview

Part I overview: Advances in our understanding of tectonic processes and associated lithospheric structure have often relied on remote sensing geophysical methods and, in particular, seismology. In regions where crustal basement rocks are concealed by thick sequences of sedimentry strata, as in southern Alberta, the use of such methods is essential if the tectonic evolutionary history is to be uncovered. The work presented in Part I of the thesis discusses a teleseismic experiment for which the objective was to obtain constraints on the lithospheric structure of southern Alberta, and to better understand the region's tectonic evolution.

2.1 Motivation and Research Goal

The formation of the supercontinent Laurentia, the Paleoproterozoic (ca. 2.0-1.6 Ga) landmass which forms the cratonic root of present day North America, is not well understood and numerous questions pertaining to the assembly of its constituent tectonic fragments (e.g., *Hoffman* [1988]) remain unresolved. One particularly enigmatic region is southern Alberta where sedimentary cover precludes direct investigation of the crustal basement. Some of the first observations relating to the region's tectonic evolution emerged from early studies of sedimentary strata [*Deiss*, 1941] which indicated an anomalous history of epeirogenic motion. Vertical movements of crustal blocks of the order of 100's of km in horizontal extent were noted, suggesting a deep, possibly subcrustal, origin. Pioneering seismic reflection studies [*Kanasewich and Cumming*,

1965; *Kanasewich et al.*, 1969; *Clowes and Kanasewich*, 1972] and early refraction studies (e.g., *Chandra and Cumming*, [1972]) further documented dramatic variations in crustal structure between the various basement domains.

During the past decade, research undertaken as part of LITHOPROBE's Alberta Basement Transect has provided better constrained and more detailed interpretations of the tectonic evolution of much of the region's crustal basement (e.g., *Eaton et al.*, [1999]; *Ross et al.*, [2000]; *Gorman et al.*, [2001]; *Lemieux et al.*, [2000]). However, one issue which remains poorly understood is the role of the subcrustal lithosphere in the formation and subsequent evolution of southwestern Laurentia. The limited depth penetration and frequency bandwidth of crustal seismic reflection profiling preclude a comprehensive examination of the region's upper mantle (i.e., to depths exceeding 150 km; see *Eaton et al.*, [2000]). Large-scale refraction profiling (e.g., DEEP PROBE) has been more successful in constraining upper mantle velocity variations (e.g., *Gorman et al.*, [2001]), although it is still limited by signal penetration in depth. Regional-scale, broadband teleseismic investigation does not suffer from these limitations to the same extent and is able to extend the resolution of velocity structure through the entire upper mantle column. Thus, the objective of the present study is to improve our current understanding of deep-seated lithospheric structure in southern Alberta through the application of a suite of teleseismic processing techniques to data recorded on a portable broadband seismic array (Chapter 3). This information will, in turn, provide additional geophysical contraints on the tectonic evolution of southern Alberta (Chapter 4).

2.2 Tectonic Overview of the Alberta Basement

The Hearne Province is one of several microcontinental fragments constituting the Laurentian supercontinent and has been geologically mapped where exposed in the Canadian Shield of Saskatchewan and the Northwest and Nunavut Territories (e.g., *Bickford et al.*, [1994]). A comprehensive understanding of its basement architecture and evolution in southern and central Alberta, western Saskatchewan, and northern Montana has, however, been hindered by the overlying Phanerozoic Western Canada Sedimentary Basin. Some information concerning the region's crustal basement is afforded by geochronological dating of drill core and potential field mapping which reveal a heterogeneous mosaic of predominantly Archean-aged crustal blocks [*Ross et al.*, 1991; see Figure 2.1].

At present, however, there is a lack of consensus concerning the tectonic affiliations of these internal blocks. In particular, the location of the boundary between the Hearne Province and the Wyoming Province to the south is in question. Some authors associate the Medicine Hat Block (MHB) with the Hearne Province (e.g., *Ross et al.*, [1991]) and propose the Great Falls Tectonic Zone as the site of the Hearne-Wyoming suture (e.g., *O'Neill and Lopez*, [1985]). Other investigators associate the MHB with the Wyoming Province (e.g., *Hoffman*, [1990]) and interpret the Vulcan Structure to represent the interprovincial suture (e.g., *Eaton et al.*, [1999]). Furthermore, geophysical evidence does not preclude the MHB from once existing as an autonomous Archean crustal fragment that is now delineated by sutures with both the Hearne and Wyoming Provinces at the Vulcan Structure and the Great Falls Tectonic Zone, respectively [*Gorman et al.*, 2001]. The tectonic relation between the MHB and its neighbouring domains is rendered still more enigmatic by observations of differential subsidence along its northern margin as revealed through changes in facies and thickness patterns identified in early stratigraphic studies (e.g., *Deiss*, [1941]).

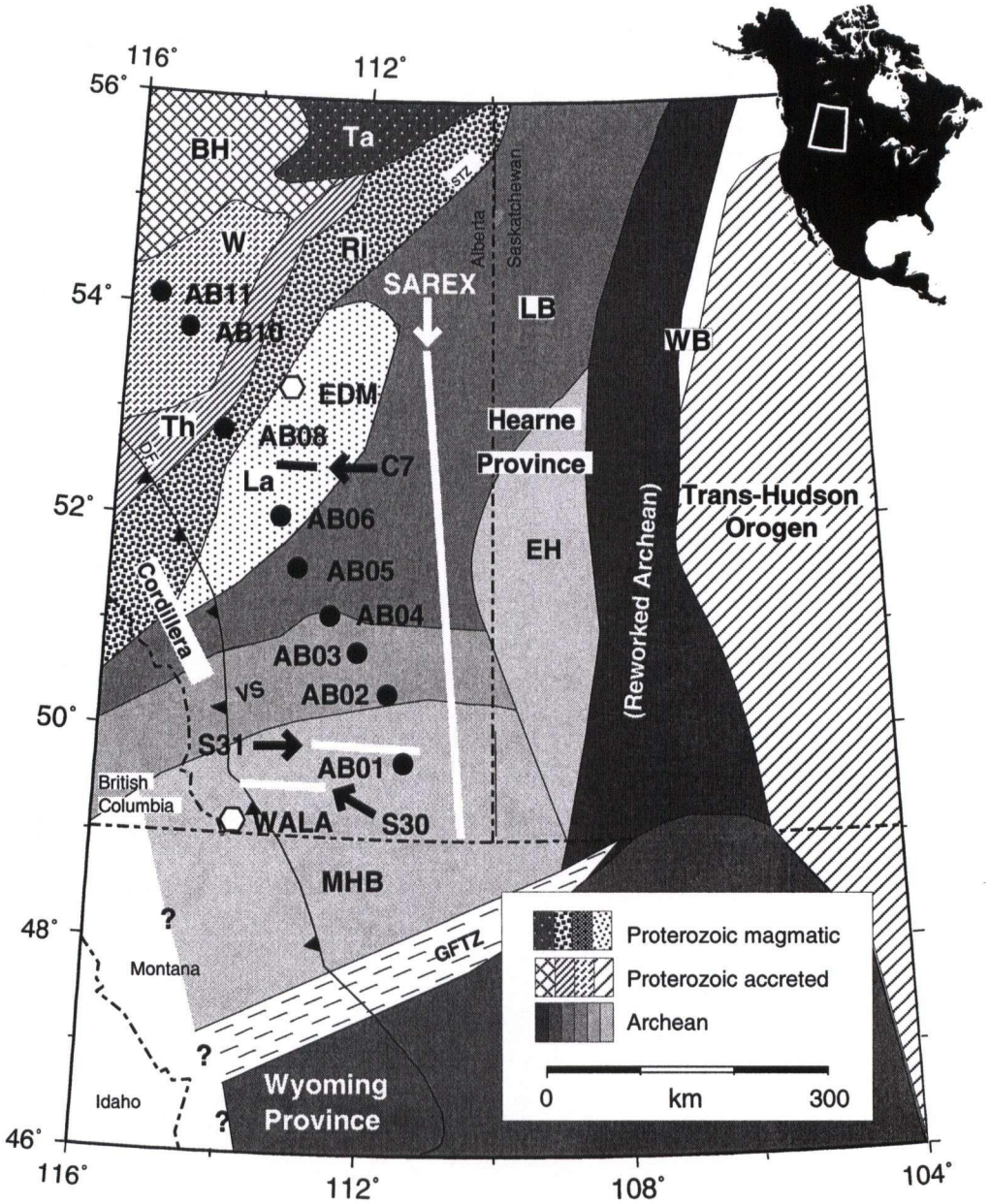

Figure 2.1: Simplified tectonic map of the study area (after *Ross et al.*, [1991]) and locations of teleseismic stations. Circles and hexagons represent portable and CNSN stations, respectively. Labelled domains: BH - Buffalo Head, EH - Eyehill High, GFTZ - Great Falls Tectonic Zone, La - Lacombe Domain, LB - Loverna Block, MHB - Medicine Hat Block, Ri - Rimbey Arc, STZ - Snowbird Tectonic Zone, Ta - Taltson Magnetic Arc, Th - Thorsby Magnetic Low, VS - Vulcan Structure, W - Wabamun Domain, WB - Wathamun Batholith. Labelled relevant active-source profiles: C7 - CAT line 7, S30 - SALT line 30, S31 - SALT line 31. Black line (with triangles) shows limit of the Cordilleran Deformation Front (DF).

The eastern margin of the Hearne Province is marked by the Trans-Hudson Orogen, a complex Paleoproterozoic orogenic belt that developed during relative convergence of the Superior and Hearne Provinces in the interval 1.9-1.7 Ga. Tectonic activity along this boundary included inward-dipping plate consumption and the subsequent imbrication of continental margin rocks beneath the Hearne Province ca. 1.85-1.78 Ga [*Ross et al.*, 2000]. The province's northwestern boundary is marked by the Snowbird Tectonic Zone, a distinct potential field anomaly which, based on constraints from recent crustal reflection profiling and long period electromagnetic surveys, has been interpreted as a lithospheric-scale Proterozoic suture zone [*Ross et al.*, 1991; 2000]. Tectonic modelling and geochronologic dating of this zone further suggest a southeastward subduction of oceanic crust beneath the Hearne Province coeval with activity along its eastern boundary. The western portion of the composite Hearne-Wyoming system is proposed to have later rifted, thus establishing a passive continental margin which was further modified through the development of the overlying North American Cordillera (e.g., *Burchfiel et al.*, [1992]). For more detail the reader is referred to *Ross et al.* [2000], *Eaton et al.* [1999], and references therein.

2.3 Previous Geophysical Coverage

Southern Alberta has long been a focus of geophysical study. Early investigation of the Vulcan Structure, including one of the first crustal seismic reflection profiles, led to the initial interpretation of this domain as a Precambrian rift on the basis of vertical offset in deep reflecting horizons and a pronounced linear anomaly in gravity and magnetic map signatures which suggested an east-west oriented graben structure [*Kanasewich et al.*, 1969]. Further geophysical constraints were supplied by *Clowes and Kanasewich* [1972] and *Chandra and Cumming* [1972] who presented evidence for varying Moho topography based on significant lateral changes in lower crustal reflection horizons, and spatial correlations between high-velocity zones at shallow crustal levels

and Bouguer gravity highs, respectively.

In the past decade, an improved understanding of the region's architecture and tectonic evolution has emerged through the multidisciplinary LITHOPROBE Alberta Basement Transect. The Central Alberta Transect (CAT), a collection of ten rectilinear, predominantly east-west profiles at ~53°N, displays crustal-scale imbrication of central and western portions of the Hearne Province with northwest vergence [*Ross et al.*, 1995]. The Trans-Hudson Orogen Transect (THOT), which profiles the northeastern sections of the Hearne Province, recorded vergence in an opposing sense [*Lucas et al.*, 1993; *Lewry et al.*, 1994]. Collectively, these two profiles document the penetrative nature of the crustal-scale Paleoproterozoic shortening of the Hearne Province [*Ross*, 1997]. Southern Alberta Lithosphere Transect (SALT) profiles, which cross from the southern Loverna Block into the northern MHB, show crustal thickening within and southward of the Vulcan Structure, and an interpreted south-verging underthrusting of the Vulcan Structure by the Loverna Block [*Eaton et al.*, 1999]. Examination of data from the Southern Alberta Refraction EXperiment (SAREX), a north-south profile situated east of the SALT lines (~110°E), reveals wavy undulations in the Loverna Block's velocity structure and a thick high velocity, lower crustal layer below the MHB [*Clowes et al.*, 2001].

Subcrustal lithospheric structure beneath southern Alberta has been illuminated by the Vibroseis Augmented Listen Time (VAuLT) experiment, a set of seismic reflection profiles which span southern Loverna Block, the Vulcan Structure, and northern MHB between ~113° and 114°E [*Eaton et al.*, 2000]. Processed VAuLT sections document south-dipping reflectivity into the upper mantle under the Loverna Block and Vulcan Structure that becomes subhorizontal beneath the MHB. This reflectivity has been interpreted to arise from compositional layering and (or) zones of ductile deformation within the mantle [*Eaton et al.*, 2000]. To the east of the VAuLT lines, these three domains have been investigated by the continental-scale refraction experiment DEEP

PROBE. The resulting profiles document two north dipping reflectors in the mantle that are interpreted to be associated with ancient subduction zones, one located to the north of the MHB, the other to the south [*Gorman et al.*, 2001]. The interpretation of a north-dipping subduction-suture zone at the Vulcan Structure may, however, be somewhat inconsistent with the south-verging reflectivity patterns noted in SALT and VAuLT profiles [*Eaton et al.*, 1999; 2000]. Mantle velocity structure elucidated by DEEP PROBE refraction profiling documents a marginally faster subcrustal mantle beneath the Hearne Province (8.2 km s^{-1}) relative to the MHB (8.1 km s^{-1}). This difference, however, diminishes at depths greater than ~80 km.

The lithospheric mantle of southern Alberta has also been characterized at greater scales using long-period seismology. Surface wave tomography [*van der Lee and Nolet*, 1997; *Frederiksen et al.*, 2001], which recovers smooth three-dimensional (3-D) regional velocity structure at length-scales greater than ~200 km, shows southern Alberta to lie within the transition between the slower (~-8%) North American Cordillera in the west and the faster (~8%) Canadian Shield region in the east. In addition, diminishing seismic velocities are noted in both of these investigations to the south of the 49°N parallel. Lithospheric conductivity structure across the Loverna Block and Proterozoic terranes to the northwest is constrained by the inversion of transverse magnetic mode magnetotelluric data [*Boerner et al.*, 1999]. Mantle conductivity profiles appear to be dominantly 2-D and characterized by anomalously high values beneath the Loverna Block which have been interpreted to reflect tectonically induced metasomatism.

2.4 Author's Contribution

The research presented in Part I of this thesis has been submitted to the *Canadian Journal of Earth Sciences* in the form of a manuscript entitled *Integrated teleseismic studies of the southern Alberta*

upper mantle on behalf of myself as principal author and my co-authors Michael Bostock, Charly Bank, and Robert Ellis. Michael Bostock and Robert Ellis conceived, designed, and oversaw the operation of the field experiment. The data set used in the present analyses was collected by field technician Aaron Webb between July 1998 and June 1999. The data were processed by myself during the same time period with Charly Bank rendering invaluable technical assistance. All of the analysis and tectonic interpretation presented in Chapters 3 and 4 was carried out by myself, although co-authors have been involved, to varying degrees, in consultative roles.

Chapter 3

Teleseismic analysis: data, techniques, and results

Chapter overview: This chapter begins with a brief summary of some of experimental data aquisition parameters and the teleseismic event data set. This is followed by a discussion of the data processing for each of three analyses: i) travel time tomography; ii) shear wave splitting; and iii) radial component receiver functions.

3.1 Data Acquisition

The data considered in this experiment were recorded between July 1998 and June 1999 on a portable array of 9 broadband (i.e., ~0.033-5.0 Hz frequency) seismographs and two permanent stations from the Canadian National Seismic Network (CNSN) at Waterton Lakes (WALA) and Edmonton (EDM), Alberta (see Figure 2.1). The array was oriented approximately perpendicular to the inferred basement strike with an interstation spacing between 40 km and 80 km. This aperture and station interval afford resolution in tomographic studies between 66 and 400 km depth in the mantle, and permit along-array profiling of upper mantle anisotropy, Moho depth, and effective Poisson's ratio of the crustal column. The array was well situated with respect to global seismicity; specifically, it falls within 100° epicentral distance from subduction zones of the northwestern Pacific, Central and South America, and much of the mid-Atlantic ridge, and Alpine-Himalaya belt. The epicentres of the earthquakes used in the analyses are plotted in Figure 3.1, and a full catalogue of events is given in Appendix A.

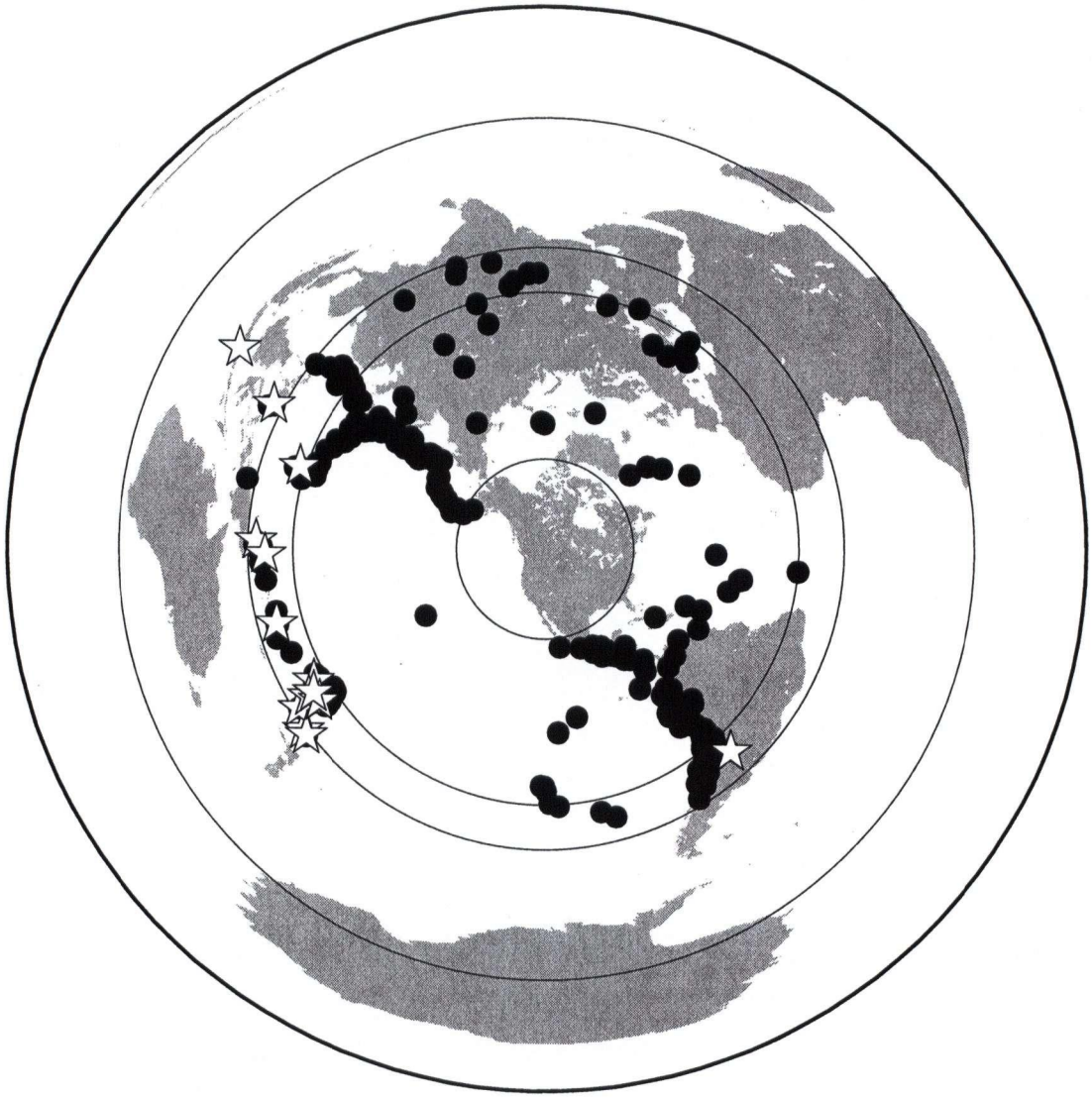

Figure 3.1: Distribution of the sources used in the analyses of Part I of the thesis. Circles and stars represent events used in *P*-wave tomography and shear-wave splitting, respectively. Events employed in receiver function analysis are comprised of a subset from both categories.

3.2 Travel Time Inversion

3.2.1 Method

Teleseismic body-wave travel times were inverted to recover a smooth, three-dimensional (3-D) model of *P*-velocity perturbations in the upper mantle beneath the area of study. The tomographic

method of *VanDecar* [1991] was employed and can be summarized as follows. Optimum delay times are determined using a multi-channel cross-correlation technique that improves visual first *P*-arrival picks by a least-squares minimization of the inconsistency between cross-correlation derived relative delay times for all pairs of stations recording a given event [*VanDecar and Crosson*, 1990; *VanDecar*, 1991]. These travel-time residuals are subsequently inverted for velocity perturbations with respect to the *iasp91* radial earth model [*Kennett and Engdahl*, 1991], beneath the array. Velocity perturbations are parameterized over a regular grid of knots every 1/3° in latitude, 1/2° in longitude, and 33 km in depth using splines under tension to smooth variations between knots. Robust linear inversion is performed using conjugate gradients (e.g., *Hestenes and Stiefel*, [1952]) combined with iterative downweighting of large residuals [*Bostock and VanDecar*, 1995] to simultaneously solve for slowness perturbations, station-time corrections (associated with e.g. topography), and event mislocation. Regularization is enforced by a damped least-squares procedure in which a combination of the first and second derivatives (flattening and smoothing) is minimized. Further information concerning the method is detailed in *VanDecar* [1991].

3.2.2 Data Set

The raw tomographic data set comprised 1565 visual travel time picks from 293 events with source magnitudes between m_b=4.4 and m_b=6.6. These times were measured primarily for direct *P*, although some core diffracted *P*-phases were also included. Cross-correlation derived relative delay times were characterized by a standard deviation of 0.023 s. The majority of events (162 out of 293) occurred in the northwestern Pacific and Latin American subduction zones, and lie within 15° of the great circle passing through the array.

3.2.3 Results

To evaluate the resolution afforded by the data set, a "checkerboard" test was performed using a synthetic model in which every fifth knot in latitude and fourth knot in longitude at three depths (133 km, 300 km, 466 km) was assigned an alternating $\pm 5\%$ slowness perturbation. Synthetic travel time residuals for the source-receiver combinations represented in the real data set were then computed, corrupted by additive Gaussian noise with standard deviation σ=0.1 s, and used as input to the inversion procedure described above. Results of the resolution test are presented in Figure 3.2. The top 66 km of the recovered model are masked out due to the incorporation of crustal and shallow mantle structure within station correction terms [*VanDecar*, 1991]. Moreover, model regions characterized by poor ray coverage and resolution are also masked out. The important features of the model, shown in Figures 3.2b,d,f,h, may be summarized as follows: i) anomalies are smeared across the array axis indicating that resolution is poorer across-axis than along-axis; ii) substantial vertical smearing exists along dominant ray directions especially near the ends of the array; and iii) recovered peak anomaly magnitudes underestimate the maximum slowness perturbations of the synthetic model. Overall, resolution in the upper 300-400 km is good, and we can expect to resolve any larger-scale mantle velocity variations underlying the major crustal domains.

Results from inversion of the real travel time data are presented in Figure 3.3 as a series of horizontal depth slices and a vertical profile A-A' through the preferred model. This model sits at the corner of the tradeoff curve between data misfit and model variance as constructed through a number of inversions involving varying combinations of candidate flattening and smoothing values. Iterative inversion of the data set led to a 66% reduction in the travel time residuals (r.m.s. reduction from 1.75 s to 0.59 s). The recovered slowness anomalies display a range of $\pm 1.7\%$ with

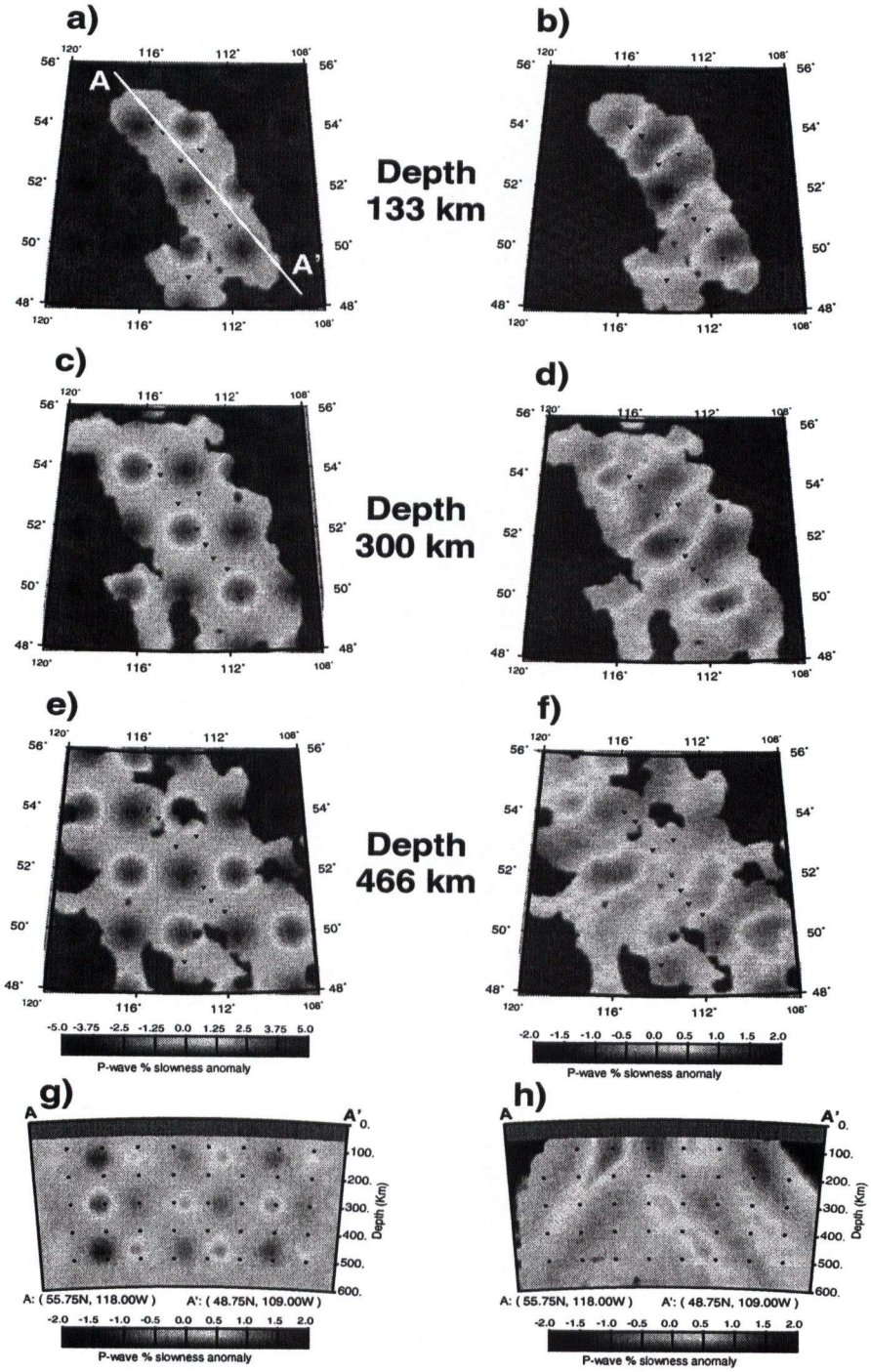

Figure 3.2: Results from a synthetic resolution test. Test involved three layers of alternating spikes with slowness perturbations of $\pm 5\%$. a) and b) synthetic model and recovered structure for spike layer at 133 km depth; c) and d) as in panels a) and b) but at 300 km depth; e) and f) as in panels a) and b) but at 466 km depth; g) and h) depth cross section along receiver array between points A and A'.

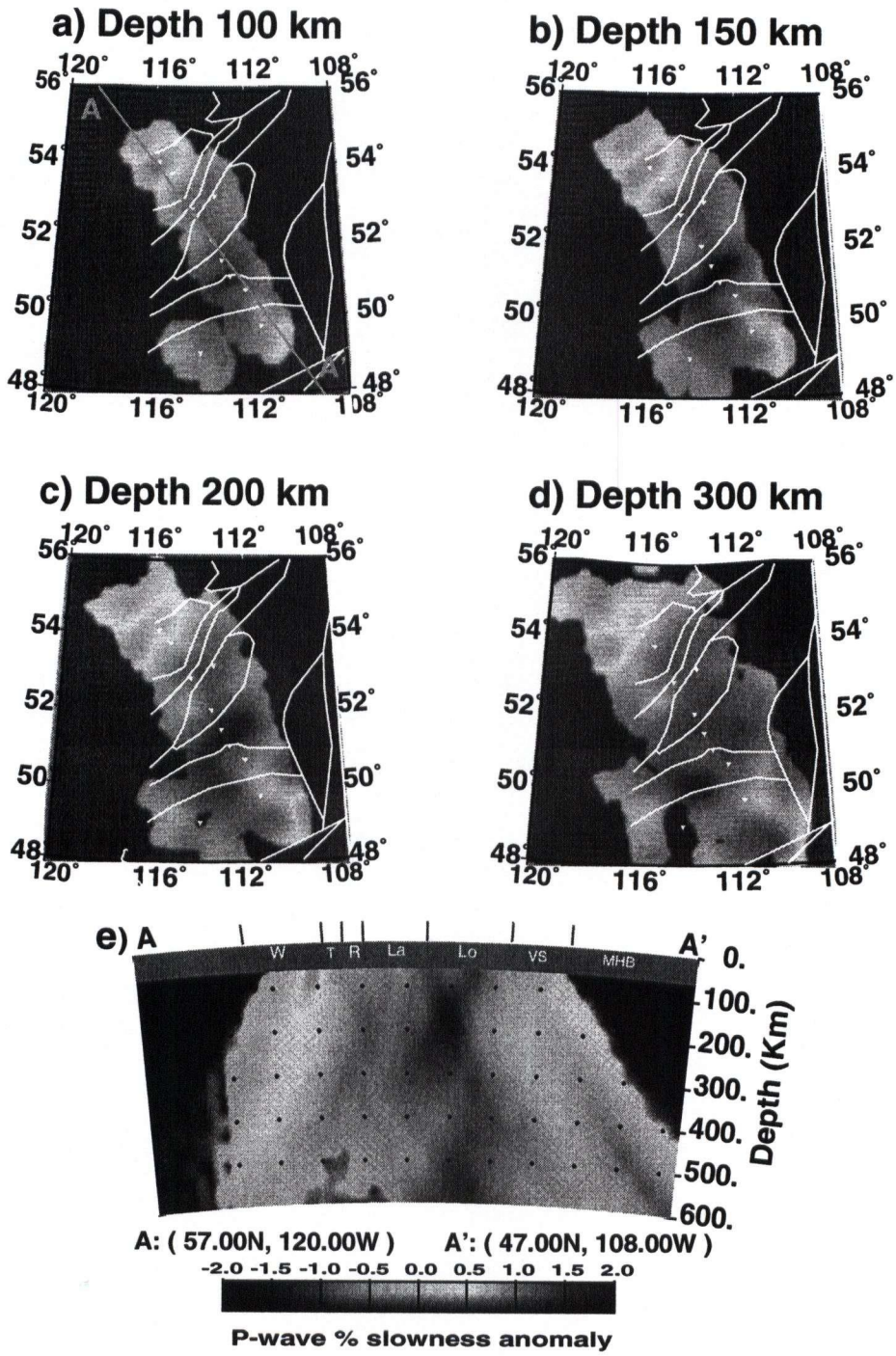

Figure 3.3: Results from travel-time tomography. a) 100 km depth; b) 150 km depth; c) 200 km depth; d) 300 km depth; e) depth cross section along array between points A and A'. Domain names given in Figure 2.1. Receiver locations used in this study shown as white triangles.

respect to the *iasp91* reference model. The most prominent feature imaged is the ~-1.7% slowness anomaly centred beneath the Loverna Block. This structure is truncated by slightly positive slowness perturbations to the south beneath parts of the Vulcan Structure and northern MHB and to the northwest where the lowest velocities are imaged below the Wabamun domain. Based on resolution tests, the localization of the largest perturbations within the top 300 km is probably robust and reflects lithospheric structure. Velocity anomalies at greater depths are, however, most certainly smeared.

3.3 Shear Wave Splitting

3.3.1 Method

Anisotropy in the continental mantle lithosphere is generally thought to develop through preferred orientation of olivine crystals in reponse to ductile deformation (e.g., *Silver and Chan* [1991]). The teleseismic *SKS*-phase affords a means of characterizing this anisotropy through the birefringence (or splitting) of *S*-waves in anisotropic material. Under the assumption of a single homogeneous layer of anisotropic mantle, the splitting of an incident *SKS*-wave into two orthogonally polarized waves may be parameterized by the polarization direction, ϕ, of the fast wave and the delay time, δt, between the two split arrivals. Parameters ϕ and δt are thereby representative of the orientation and degree of anisotropy, respectively.

The analysis method employed in the present study is adopted from *Silver and Chan* [1991] and is illustrated in Figure 3.4. Windows about the *SKS*-arrival on the horizontal (north and east) traces are selected (Figures 3.4a,b) and the waveforms are subsequently rotated into radial and transverse components (Figures 3.4c,d). These components are rotated through a trial angle ϕ (Figures 3.4e,f) and shifted by a time delay δt (Figures 3.4g,h) in an attempt to correct for the

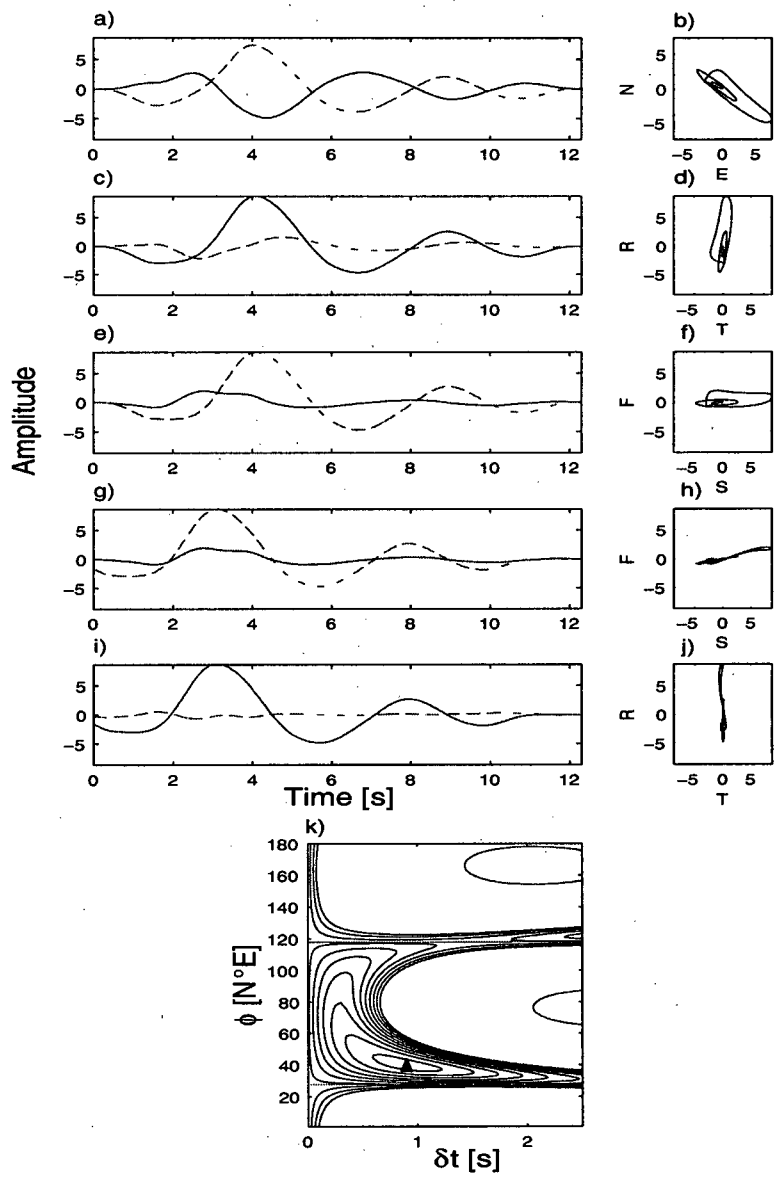

Figure 3.4: Example of shear wave splitting processing. Event 98/09/02 08:37.29 recorded at station AB04 (back azimuth 297.87, epicentral distance 104.19). a) north (solid line - SL) and east (dashed line - DL) component *SKS* arrival picks; b) particle motion diagram of panel a); c) and d) as in panels a) and b) but rotated into radial (DL) and transverse (SL); e) and f) are components shown in panels c) and d) rotated by trial ϕ into fast (DL) and slow (SL) components; g) and h) are components shown in panels e) and f) shifted by trial time δt; i) and j) are the anisotropy corrected components shown in panels g) and h) rotated back into radial (SL) and transverse (DL) components; k) contour map representing minimization of transverse component energy of panels i) and j) as function of candidate $[\phi, \delta t]$ values. Global minimum shown as triangle; quoted error value outlined by enveloping nearest contour.

magnitude and direction of anisotropy manifest in the recorded signals. From these 'corrected' traces (Figures 3.4i,j) estimates of two functions (the energy on the transverse component and the second eigenvalue of the covariance matrix formed from the two split waves; see, e.g., *Silver and Chan*, [1991]) are obtained to serve as measures of the success of a particular $\phi,\delta t$ pair in accounting for anisotropy as manifest on the transverse component. This procedure is then repeated through iteration over a range of candidate ($\phi,\delta t$) values to find the two-parameter pair which minimizes these energy measures (Figure 3.4k). This method has been extended through a simultaneous accommodation of multiple measurements to improve the accuracy of the splitting parameter estimates [*Wolfe and Silver*, 1998] and this extension has been adopted here.

3.3.2 Data Set

A total of 14 earthquake sources yielding 31 station-events were used in the *SKS*-splitting analysis. Contained within this suite of events were six m_b >5.8 earthquakes procured for stations EDM and WALA from the CNSN archives. Stations AB02, AB03, AB06, and AB10 failed to record any *SKS*-phases at sufficient signal-to-noise levels to merit investigation. An examination of the epicentral distance coverage of the fourteen earthquakes used in the present analysis (shown as stars in Figure 3.1) indicates that the large majority of events originated from the western Pacific (back azimuth ~230-300°), with a single suitable earthquake from South America (back azimuth ~140°). The limited geographical sampling of these events does not permit evaluation of the dependence of splitting parameters on back azimuth; thus, it is necessarily assumed that lithospheric mantle anisotropy is homogeneous, with hexagonal symmetry and horizontal symmetry axis.

3.3.3 Results

Results from multi-event *SKS* splitting analysis are presented in Table 3.1 and Figure 3.5. The average value of ϕ over the entire array is 45±8°, with individual results ranging between 39±8° and 55±8°. The fast direction at station AB08 is rotated slightly clockwise of the relatively uniform northeast polarization direction calculated at other northern stations of the array, but this may reflect larger errors due to the small number of observations (2) at this station. Variations

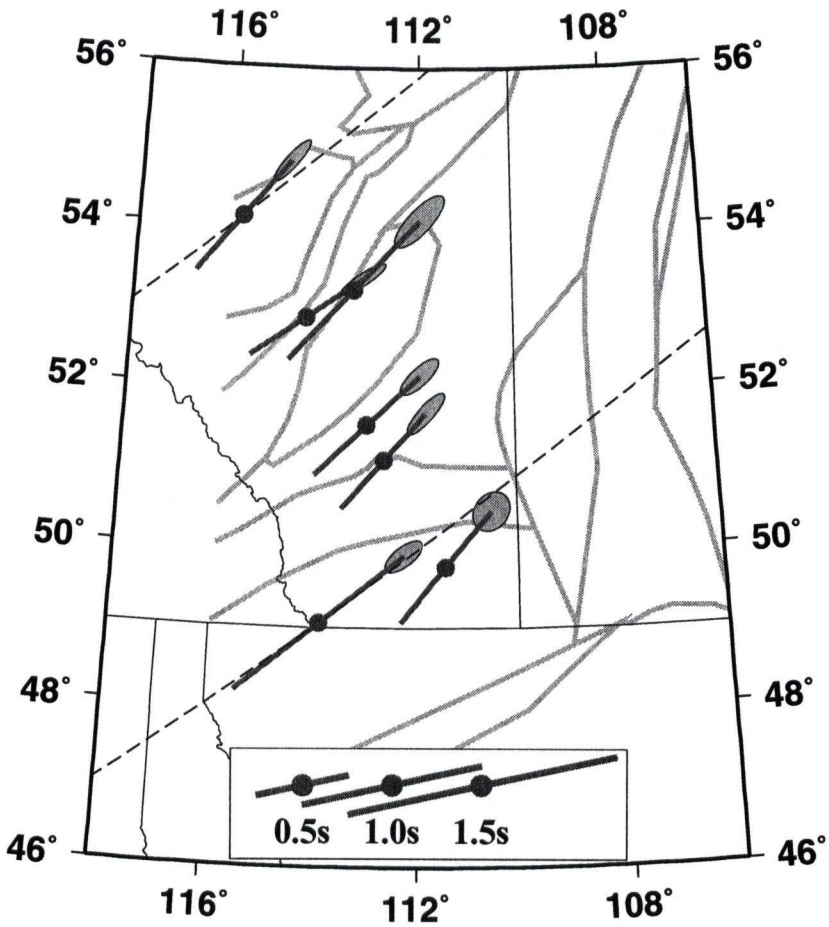

Figure 3.5: Results (direction and magnitudes) of shear wave splitting analysis. Ovals and dotted line indicate estimated uncertainty ranges and absolute plate motion direction [*Minster and Jordan*, 1978], respectively. Domain names given in Figure 2.1.

in splitting magnitude recorded at the six northern reporting stations range moderately uniformly between 0.70±0.30 s and 1.05±0.38 s (average 0.82±0.30 s). The remaining station, WALA, displays a slight increase in splitting delay time magnitude (1.20±0.30 s) and a clockwise rotation in polarization angle (ϕ=53±7°) possibly reflecting its proximity to Cordilleran deformation. Shear-wave splitting measurements for EDM and WALA have also been published by *Bostock and Cassidy* [1995] who obtain 33° and 0.6 s, and 37° and 0.9 s for these two stations, respectively (no uncertainty estimates given). Assuming uncertainties comparable to those of this study, these measurements are found to agree to within statistical error.

Table 3.1: Station locations and results of shear wave splitting and receiver function analyses.

Stat	lat °N	lon °W	Split data	ϕ [°]	δt [s]	Moho data	Moho depth [km]	Poisson's Ratio
WALA	49.06	113.91	8	53±7	1.20±0.30	34	50.0±2.0	0.26±0.02
AB01	49.77	111.43	2	40±13	0.80±0.23	19	42.5±2.0	0.29±0.02
AB02	50.34	111.73	-	-	-	-	-	-
AB03	50.73	112.06	-	-	-	10	38.0±2.0	0.30±0.03
AB04	51.10	112.68	4	42±7	0.70±0.30	-	-	-
AB05	51.54	113.04	3	47±7	0.80±0.28	37	37.8±2.0	0.30±0.02
AB06	52.05	113.44	-	-	-	3	38.0±3.0	0.30±0.03
AB08	52.87	114.34	2	55±5	0.75±0.30	5	37.8±3.0	0.28±0.03
EDM	53.22	113.35	8	43±7	1.05±0.38	32	37.3±2.5	0.28±0.03
AB10	53.81	115.21	-	-	-	-	-	-
AB11	54.12	115.76	4	39±5	0.80±0.30	48	37.8±2.0	0.29±0.02

3.4 Receiver Function Analysis

3.4.1 Method

Receiver function analysis exploits information contained in the teleseismic *P*-wave coda to study discontinuities in the crust and upper mantle (e.g., *Langston*, [1979]). The approach adopted here is illustrated in Figure 3.6 and follows the method of *Bostock* [1998] which may summarized as follows. The three components of ground displacement are transformed into estimates of the *P*, *SV*, and *SH* wavefields using estimates of near-surface *P*- and *S*-velocities and the wavefront slowness. Wavefields from sources of similar epicentral distance and back azimuth (Figures 3.6a,b,c) are processed together in a simultaneous least-squares deconvolution of *S*-components by *P*-components to estimate the Earth's impulse response (Figure 3.6d).

The receiver functions can be further processed to yield estimates of crustal thickness and Poisson's ratio [*Zhu and Kanamori*, 2000]. Employing an average crustal *P*-wave velocity of 6.5 km s^{-1}, the binned receiver function amplitudes, at times corresponding to the direct (or Moho) conversion and the two first-order crustal reverberations (weighted by factors of 0.5, 0.3, and -0.2 respectively), are summed over a range of candidate Moho depths and crustal Poisson's ratios to locate the two-parameter combination which results in maximum coherence (Figure 3.6e). Uncertainty estimates in the present analysis are determined from the contour level of these stacks at 90% of the maximum value.

3.4.2 Data

The data chosen for receiver function analysis at each station consisted of up to 48 seismograms (see Table 3.1) with individual traces selected on the basis of signal-to-noise levels. These events

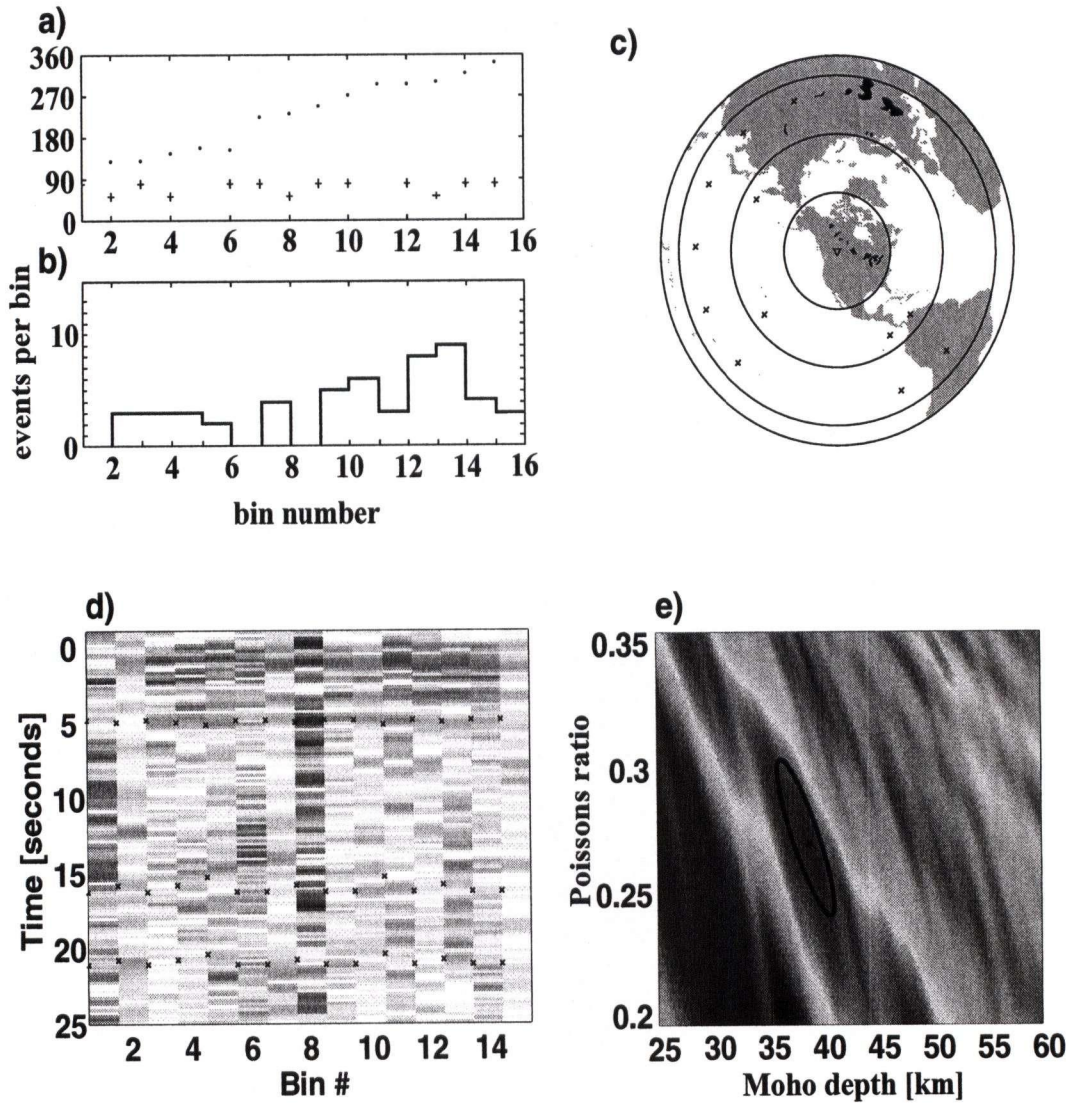

Figure 3.6: Examples of receiver function processing for station EDM. a) location of bins as a function of back azimuth (.) and epicentral distance (+); b) number of events per bin; c) corresponding locations of bins in panels a) and b); d) sample receiver functions with best fit locations of direct *P-S* conversion and two first-order free-surface multiples (x); e) summed energy magnitude as function of candidate Poisson's ratio and Moho depth values with oval representing boundary of values falling with 90% of global maximum.

represent subsets of the suite of earthquakes employed in *P*-wave travel-time inversion and (or) shear-wave splitting analyses.

3.4.3 Results

Estimates of Moho depth and bulk crustal Poisson's ratio obtained from receiver function analysis for eight stations are presented in Table 3.1. Moho depths at the six northern reporting stations are fairly uniform exhibiting an average value of $\sim 38 \pm 2$ km. Stations AB01 and WALA, located in the MHB, display a deeper Moho signature at 42.5 ± 2 km and 50 ± 2 km, respectively. Poisson's ratio estimates are also fairly uniform with an average value (0.28 ± 0.02). Station WALA again deviates from the regional trend with a result that is slightly lower than those to the north and east. Parameter values at both CNSN stations (EDM and WALA) have been checked against a much larger selection of events (>100) from CNSN archives with similar results (*Bank*, Ph.D. thesis in preparation).

Chapter 4

Implications for southern Alberta's tectonic history

Chapter overview: This chapter discusses contraints on southern Alberta lithospheric structure and evolution that have arisen from the analyses presented in Chapter 3. In particular, aspects of the tectonic history of the Loverna and Medicine Hat Blocks, the origin of lithospheric anisotropy, and Moho depth and bulk crustal Poisson's estimates beneath individual stations are examined.

4.1 Discussion

The inversion of *P*-wave traveltime data from south-central Alberta has imaged significant lateral variations in mantle velocity structure. These variations appear to correlate with inferred locations of crustal basement domains, and are most prominent within the top 100-200 km of the mantle. In Figure 4.1, we plot the relative slowness perturbation at 133 km depth as an indication of velocity trends beneath the array. The lowest velocities (highest slownesses) are identified towards the northern (Wabamun Domain) and southern (MHB) ends of the array with highest velocities (lowest slownesses) located beneath the Loverna Block. Localization of the strongest velocity anomalies to the upper ~200 km of the mantle is taken to reflect the preservation of fossil heterogenity in a relatively rigid lithosphere. Accordingly, the highest velocities beneath the Loverna Block are interpreted to be structurally significant, and representative of the thickest lithosphere documented along the profile.

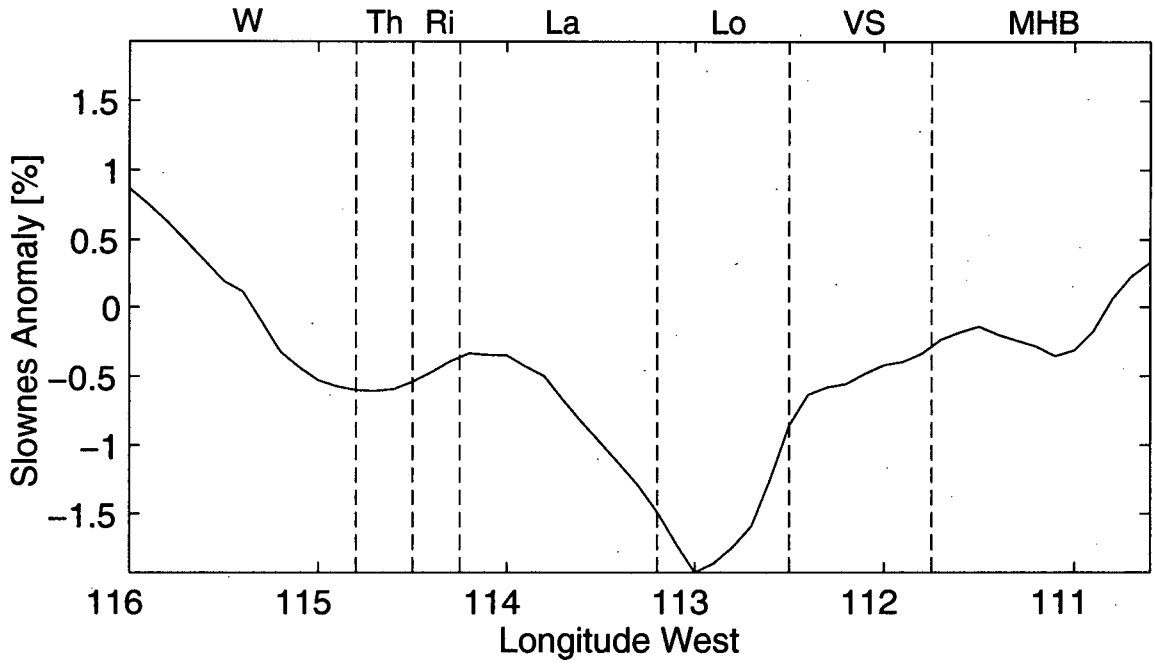

Figure 4.1: Along-array profile of *P*-wave velocity model at 133 km depth. Documented profile contained within A-A' of Figure 3.3. Domain abbreviations as in Figure 2.1.

These observations present some problems for a recent model [*Ross et al.*, 2000] of mantle evolution beneath the Hearne Province. In this model, the contemporaneity of two inward-dipping subduction zones, one involving young buoyant oceanic lithosphere to the northwest and the other continental lithosphere to the east, led to a "tectonic vise" in which a relatively compliant Hearne Province was compressed between two more rigid lithospheric blocks. This configuration enabled underthrusting-related mechanical interaction with the sub-Hearne lithosphere causing shortening and erosion of the mantle, and possibly fostering the growth of the continental root. Soon afterwards, the newly thickened lithosphere is postulated to have been thinned or removed via convective erosion or delamination leading to asthenospheric decompression and crustal melting arising from increased heat flow. This latter inference is partly based on mantle conductivity

profiles derived from magnetotelluric measurements which indicate substantially more conductive mantle beneath the Archean Hearne province than the Proterozoic domains to the northwest [*Boerner et al.*, 1999; 2000]. The increased conductivity is thought to be due to the ingression of asthenospheric melts during decompression which may have prompted melting and related compositional modification of depleted mantle remnants.

On the basis of this tectonic model and, in particular, the inference of large-scale lithospheric removal, one might expect seismic velocities beneath the Hearne Province to be diminished with little internal variation. However, a comparison of Figure 3.3 with Figure 17 of *Boerner et al.* [2000] indicates a strong positive correlation between conductivity and velocity. Large-scale lithospheric removal is difficult to reconcile with this observation and it seems likely, therefore, that the agent responsible for enhanced conductivity has not affected the bulk elastic properties (and hence bulk composition or thickness) of the lithospheric mantle, or at least not in the manner generally expected.

The teleseismic results are therefore interpreted to indicate that mantle below the central Hearne Province was thickened but not delaminated. In particular, it is suggested that inward-directed subduction from the northwest along the Snowbird Tectonic Zone, the east along the boundary with the Trans-Hudson Orogen, and possibly the south along the Vulcan Structure [*Gorman*, 2000; but see also *Eaton et al.*, 1999] created the thickest lithosphere beneath the Loverna Block through successive imbrication of subducted lithospheres. Geophysical observations (e.g., *Hyndman*, [1988]) at modern subduction zones are often interpreted to indicate that dehydration above the slab plays an important role in modifying the overlying lithosphere. Accordingly, it is suggested that a volumetrically minor species (e.g., hydrous phases, *Boerner et al.*, [1999]; dissolved hydrogen, *Karato*, [1990]; carbon, *Roberts et al.*, [1999]) introduced through successive episodes of subduction has created a highly conductive Hearne lithosphere which, nonetheless,

is characterized by thick and high velocity lithosphere.

Another, possibly surprising, feature in the *P*-wave velocity model is the change from higher velocity beneath the Loverna Block to lower velocities beneath the northernmost MHB. This substantial variation (~2%) supports the conjecture of *Eaton et al.* [1999] that the two domains are genetically distinct and that the Vulcan Structure marks a structural suture (see also *Gorman et al.*, [2001]). However, the observation that the MHB represents a long-standing stratigraphic high is more difficult to reconcile with the velocity model. In particular, it suggests that the MHB may be underlain by mantle that is on average less dense than the surroundings, resulting in a net buoyancy. The difficulty arises in identifying plausible mechanisms. A thermal contribution would agree with the observed velocity trend (i.e., higher temperature producing lower density and lower velocity) but is deemed unlikely given typical diffusion time scales and the timing of the last episode of tectonic activity. A second possibility, increased iron depletion which characterizes ancient Archean lithospheres [*Jordan*, 1988], cannot be appealed to because, although it results in decreased density of peridotite, it is also accompanied by increased elastic wave velocities. Rather, it may be that the differential motions are related to dynamic forcing of a more distant origin involving subduction [*Pysklywec and Mitrovica*, 2000]; however, in that case there must still be regional controls on short wavelength structure. Finally, it is worth noting that continental-scale tomographic investigations [*van der Lee and Nolet*, 1997; *Frederiksen et al.*, 2001] also note a general decrease in mantle velocity southward from the Hearne Province to Wyoming Province.

The nature of lithospheric anisotropy, as inferred from the analysis of *SKS*, is thought to be closely related to an imprint of the most recent episode of tectonism to have affected a region [*Silver and Chan*, 1991]. Depth localization of anisotropy is poorly constrained since the near vertical *SKS* raypath provides only a vertical averaging of mantle fabric. One must therefore also consider the possible influence of plate motion and asthenospheric flow on the observables ϕ and

δt [*Vinnik et al.*, 1995; *Fouch et al.*, 2000]. Analysis of *SKS* waves in the present experiment has revealed a fairly uniform set of anisotropy splitting parameters. The average polarization direction corresponds approximately to both the normal to an average northwest-directed shortening in the Hearne Province [*Ross et al.*, 2000], and to the direction of North American absolute plate motion ($\phi_{apm} \sim 54°$, [*Minster and Jordan*, 1978]; the dashed line in Figure 3.5). This coincidence, as in many parts of Precambrian North America (see, e.g., *Silver and Chan*, [1991]), renders it difficult to separate relative contributions from fossil anisotropy in the lithosphere and flow in the underlying asthenosphere. However, a lack of systematic variation in splitting parameters that might correspond to the clockwise rotation in geological strike of the basement from north to south (see Figure 3.5) suggests that at least some component of the splitting signal originates in the asthenosphere.

The results from receiver function analysis in the present experiment reveal north-to-south variations in crustal thickness. Stations at the northern end of the array exhibit relatively uniform depths to the Moho of $\sim$ 38 km, whereas stations within the MHB are located over significantly thicker crust ($>$ 40 km). Although teleseismic stations and the aforementioned reflection (SALT, CAT) and refraction (SAREX) surveys are offset at points by distances in excess of 100 km (see Figure 2.1), comparisons drawn between interpreted profiles are still informative. Generally, Moho depths retrieved in the present study vary consistently with those obtained from active-source surveys. For example, station AB01 may be compared to SALT line 31 (43 km vs $\sim$47 km) and SAREX (43 km vs $\sim$48 km); station WALA to SALT line 30 (50 km vs $\sim$51 km); station AB05 to SAREX (38 km vs $\sim$45 km); and station AB06 to CAT line 7 (38 km vs $\sim$38 km). Discrepancies between Moho depth estimates may result from some combination of two factors. First, as illustrated by *Clowes et al.* [2001] in their comparison of SAREX refraction and SALT

(line 21) reflection profiles, significant variations in depth to the Moho exist along strike. Second, Moho depth estimates retrieved by the aforementioned techniques may be biased differently according to frequency bandwidth and nature of discontinuity (e.g., *Zandt and Owens*, [1986]).

Part II

INVERSION/MIGRATION OF SCATTERED TELESEISMIC BODY-WAVES: NUMERICAL MODELLING

Chapter 5

Motivation for Part II

Part II overview: Advances in our understanding of the continental lithosphere and underlying upper mantle have relied heavily on studies involving multichannel processing of teleseismic body wave data, most notably *P*-wave travel time tomography (e.g., *VanDecar*, [1991]). Recent investigations (e.g., *Revenaugh*, [1995]; *Bostock*, [1998]; *Ryberg and Weber*, [2000]), however, indicate that further insight into detailed lithospheric structure is to be obtained through multi-channel analysis of secondary scattered waves in the *P*-coda. The research presented in Part II of the thesis investigates a theoretically rigorous yet practically implementable solution to the inverse scattering/migration problem in earthquake seismology.

5.1 Overview of Method

The theoretical framework for inverse scattering/migration of teleseismic waves exploited in Part II of this thesis was developed in *Bostock et al.* [2000; hereafter referred to as *Paper I*], which is an extension of the earlier approach of *Bostock and Rondenay* [1999; hereafter referred to as *BR*]. The issue addressed in both of these works is formal, yet practical, inversion of scattered teleseismic body wave coda recorded on dense surface arrays for underlying 2-D lithospheric structure using inverse-scattering theory (see Figure 5.1). In particular, the approach is amenable to: i) irregular receiver sampling; ii) independent appraisal of contributions from individual scattering mode interactions including free-surface multiples; and iii) simultaneous treatment of multiple

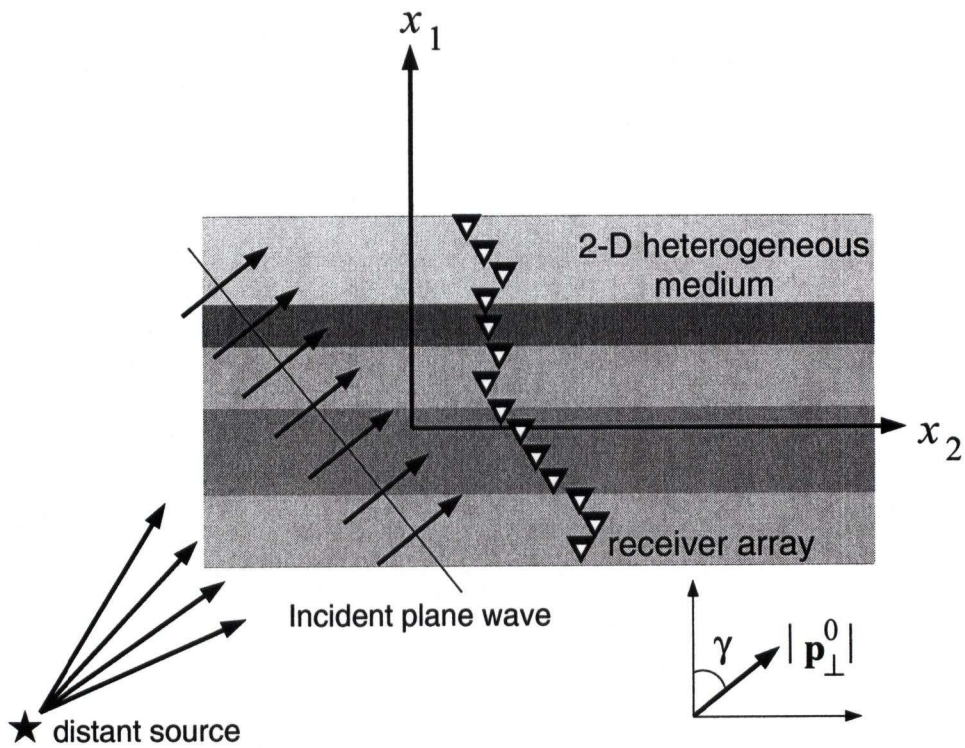

Figure 5.1: Plan view of a quasi-linear array of receivers (inverted triangles) above a 2-D heterogeneous lithosphere illuminated by an incident teleseismic wavefield. The incident wavefront is assumed to be planar at the scale of the array, with horizontal slowness $\mathbf{p}_\perp^0=(p_1^0,p_2)$, and conservation of the x_2 slowness component p_2 for all derived waves as required by Snell's law. (source: *Paper I*)

events from arbitrary back azimuths. Below I provide a necessarily brief outline of essential steps involved in the derivation of the inversion formula. Readers interested in more complete theoretical development are directed to *Paper I*.

The inversion method is based on a high-frequency, single-scattering formulation of the forward-scattering problem in which the frequency domain scattered displacement field, $\Delta u_n^q(\mathbf{x}', \mathbf{p}_\perp^0, \omega)$, from a planar (in horizontal aspect) incident wave for a particular scattering mode interaction, q (see Figure 5.2), and direction component, n, can be expressed (c.f. equation (26)

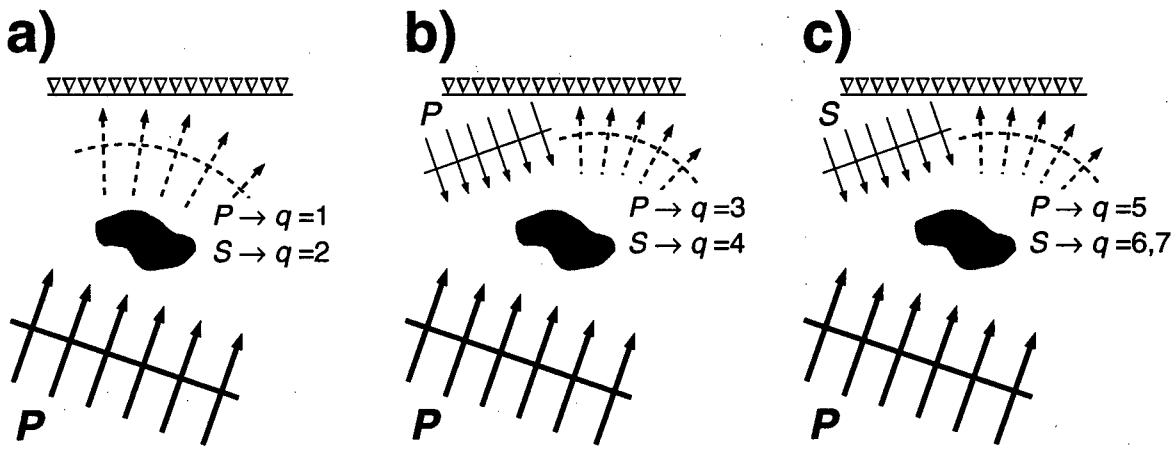

Figure 5.2: Schematic diagrams illustrating the scattering modes employed in Part II: a) forward-scattering of incident *P*-wave into *P* (q=1) and *S* (q=2) waves; b) back-scattering of free-surface-reflected *P*-wave into *P* (q=3) and *S* (q=4) waves; and c) back-scattering of free-surface-reflected *S*-wave into *P* (q=5), *S(V)* (q=6), and *S(H)* (q=7) waves. (source: *Rondenay*, [2000])

in *Paper I*) as,

$$\Delta u_n^q(\mathbf{x}', \mathbf{p}_\perp^0, \omega) = K(\omega) \int \mathrm{d}\mathbf{x}\, f^q(\mathbf{x}, \theta) \mathcal{A}_n^q(\mathbf{x}, \mathbf{x}', \mathbf{p}_\perp^0) \mathrm{e}^{\mathrm{i}\omega \mathcal{T}^q(\mathbf{x}, \mathbf{x}', \mathbf{p}_\perp^0)}, \tag{5.1}$$

where 2-D spatial variables $\mathbf{x}$, $\mathbf{x}'$ represent scatterer and receiver locations, respectively, and lie within the x_1,x_3 plane (i.e., 2-D strike parallels x_2-coordinate, with x_1 orthogonal in horizontal plane and x_3 vertical, positive downward; see Figure 5.1); and $\mathbf{p}_\perp^0$=(p_1^0,p_2) is the horizontal slowness of the incident wave. A frequency factor $K(\omega)$=$\omega^2/\sqrt{-\mathrm{i}\omega}$ arises from the planar nature of the incident wavefield and the 2-D experimental geometry. The scattering potential,

$$f^q(\mathbf{x}, \theta) = \sum_{l=1}^{3} W_l^q(\theta) \Delta m_l(\mathbf{x}), \tag{5.2}$$

includes the scattering angle θ dependent radiation pattern coefficients $W_l^q(\theta)$, and material property perturbations Δm_l=[$\Delta\alpha/\alpha, \Delta\beta/\beta, \Delta\rho/\rho$], where α, β, and ρ are the *P*-wave and *S*-wave

velocities, and density of the reference medium, respectively. Full expressions for $f^q(\mathbf{x}, \theta)$ are given in Appendix B. Quantity $\mathcal{T}^q(\mathbf{x}, \mathbf{x}', \mathbf{p}_\perp^0)$ is the arrival time at receiver $\mathbf{x}'$ of energy scattered from model point $\mathbf{x}$, and $\mathcal{A}_n^q(\mathbf{x}, \mathbf{x}', \mathbf{p}_\perp^0)$ represents the product of geometrical amplitudes of the incident and scattered waves. That is, for $q = 1$, for example,

$$\mathcal{A}_n^1(\mathbf{x}, \mathbf{x}', \mathbf{p}_\perp^0) = A^0(x_3) A^P(x_3; x_3', \mathbf{p}_\perp^0) \hat{x}_n^P(x_3', \mathbf{p}_\perp^0), \tag{5.3}$$

where $A^0(x_3)$ is the incident wavefield amplitude, and $A^P(x_3; x_3'; \mathbf{p}_\perp^0)$ and $\hat{x}_n^P(x_3', \mathbf{p}_\perp^0)$ are the amplitude and source polarization of the scattered P-wave Green's function, respectively.

At this point in the derivation, it proves expedient to introduce a new, filtered time-series, $v_n^q(\mathbf{x}', \mathbf{p}_\perp^0, t)$, through multiplication of both sides of equation (5.1) by factor $-\mathrm{i}\,\mathrm{sgn}(\omega)/\sqrt{-\mathrm{i}\omega}$ and a subsequent Fourier transform,

$$\begin{aligned} v_n^q(\mathbf{x}', \mathbf{p}_\perp^0, t) &= -\frac{1}{2\pi} \int \mathrm{d}\omega\, \mathrm{e}^{\mathrm{i}\omega t} \Delta u_n^q(\mathbf{x}', \mathbf{p}_\perp^0, \omega) \mathrm{i}\,\mathrm{sgn}(\omega)/\sqrt{-\mathrm{i}\omega} \\ &= -\int \mathrm{d}\mathbf{x}\, f^q(\mathbf{x}, \theta) \mathcal{A}_n^q(\mathbf{x}, \mathbf{x}', \mathbf{p}_\perp^0) \frac{1}{2\pi} \int \mathrm{d}\omega\, \mathrm{i}\omega \mathrm{e}^{\mathrm{i}\omega[t - \mathcal{T}^q(\mathbf{x}, \mathbf{x}', \mathbf{p}_\perp^0)]} \mathrm{i}\,\mathrm{sgn}(\omega) \\ &= -\int \mathrm{d}\mathbf{x}\, f^q(\mathbf{x}, \theta) \mathcal{A}_n^q(\mathbf{x}, \mathbf{x}', \mathbf{p}_\perp^0) \mathcal{H}\left\{\delta'\left[t - \mathcal{T}^q(\mathbf{x}, \mathbf{x}', \mathbf{p}_\perp^0)\right]\right\}, \end{aligned} \tag{5.4}$$

where $\mathcal{H}\{\cdot\}$ denotes a Hilbert transform. Note that $\delta'[t - \mathcal{T}^q(\mathbf{x}, \mathbf{x}', \mathbf{p}_\perp^0)]$ is the derivative of the singular function for the isochronal curve which defines the locus of all model points $\mathbf{x}$ from which scattered energy arrives simultaneously at receiver $\mathbf{x}'$ (See Figure 5.3).

Assuming that the scattering body is localized to the vicinity of a point $\mathbf{x}_0$, and that the amplitude function $\mathcal{A}_n^q(\mathbf{x}, \mathbf{x}', \mathbf{p}_\perp^0)$ may be approximated by $\mathcal{A}_n^q(\mathbf{x}_0, \mathbf{x}', \mathbf{p}_\perp^0)$ (i.e., that $\mathcal{A}_n^q(\mathbf{x}, \mathbf{x}', \mathbf{p}_\perp^0)$ is a slowly varying function for $\mathbf{x}_0$ near $\mathbf{x}$; see *Miller et al.*, [1987]), equation (5.4) may be rewritten as,

$$v_n^q(\mathbf{x}', \mathbf{p}_\perp^0, t) \approx \frac{\mathcal{A}_n^q(\mathbf{x}_0, \mathbf{x}', \mathbf{p}_\perp^0)}{|\nabla \mathcal{T}_0^q|^2} \int \mathrm{d}\mathbf{x}\, f^q(\mathbf{x}, \theta) \mathcal{H}\left\{\delta'\left[\mathbf{n} \cdot (\mathbf{x} - \mathbf{x}_0)\right]\right\}, \tag{5.5}$$

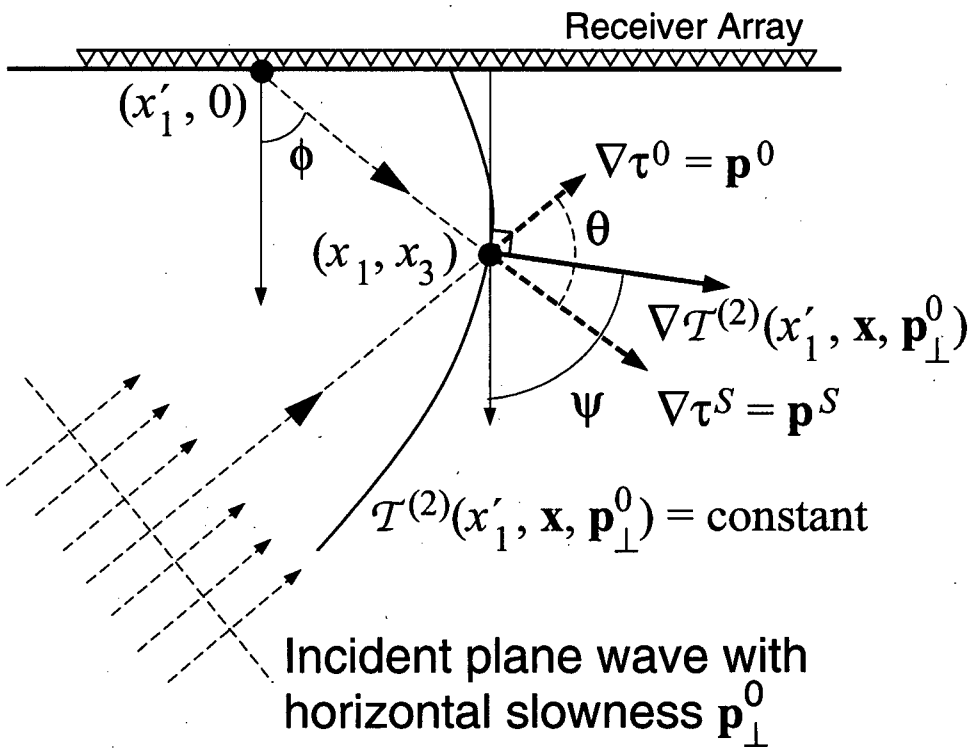

Figure 5.3: Geometrical quantities considered for scattered teleseismic waveform inversion. All quantities are projected onto the x_1-x_3 plane, and represented with solid lines when strictly confined to this plane, or with dashed lines when they have a non-zero component in the x_2 direction. (source: *Paper I*)

where $\mathcal{T}_0^q = \mathcal{T}_0^q(\mathbf{x}_0, \mathbf{x}', \mathbf{p}_\perp^0)$ is the travel time for a scattered wave from point $\mathbf{x}_0$ to receiver $\mathbf{x}'$, $\nabla\mathcal{T}_0^q$ is the spatial gradient of the total travel time function evaluated at $\mathbf{x}_0$, and $\mathbf{n} = \mathcal{T}_0^q / |\nabla\mathcal{T}_0^q|^2$ is a unit vector defining the direction of the gradient of the total travel time function (see Figure 5.3)

Contracting both sides of equation (5.5) with $\mathcal{A}_n^q(\mathbf{x}_0, \mathbf{x}', \mathbf{p}_\perp^0)$, rearranging terms, and integrating over the full range of ψ (the angle defined by the dot product of unit vector $\mathbf{n}$ with the $\mathbf{x}_3$ axis) yields,

$$-\frac{1}{4\pi}\int_0^{2\pi} \mathrm{d}\psi \int \mathrm{d}\mathbf{x}\, f^q(\mathbf{x}, \theta)\mathcal{H}\left\{\delta'\left[\mathbf{n}\cdot(\mathbf{x}_0 - \mathbf{x})\right]\right\}$$

$$= \frac{1}{4\pi} \int \mathrm{d}\psi \, \frac{|\nabla \mathcal{T}_0^q|^2}{|\mathcal{A}^q|^2} \sum_n \mathcal{A}_n^q(\mathbf{x}_o, \mathbf{x}', \mathbf{p}_\perp^0) v_n^q(\mathbf{x}', \mathbf{p}_\perp^0, t = \mathcal{T}_0^q), \tag{5.6}$$

where $|\mathcal{A}^q|^2 = \sum_n \mathcal{A}_n^q(\mathbf{x}_0, \mathbf{x}', \mathbf{p}_\perp^0)\mathcal{A}_n^q(\mathbf{x}_0, \mathbf{x}', \mathbf{p}_\perp^0)$.

Equation (5.6) is reminiscent of the definition of the inverse Radon transform [*Beylkin*, 1985] in two dimensions. The 2-D Radon transform pair is given by,

$$F(\mathbf{n}, s) = \int \mathrm{d}\mathbf{x} \, f(\mathbf{x}) \delta(s - \mathbf{n} \cdot \mathbf{x}), \tag{5.7}$$

$$\begin{aligned} f(\mathbf{x}_0) &= -\frac{1}{4\pi} \int \mathrm{d}\mathbf{n} \, \mathcal{H} \left[\frac{\partial}{\partial s} F(\mathbf{n}, s) \bigg|_{s=\mathbf{n}\cdot\mathbf{x}_0} \right] \\ &= -\frac{1}{4\pi} \int \mathrm{d}\mathbf{n} \int \mathrm{d}\mathbf{x} \, f(\mathbf{x}) \mathcal{H} \left\{ \delta' \left[\mathbf{n} \cdot (\mathbf{x}_0 - \mathbf{x}) \right] \right\} \\ &= -\frac{1}{4\pi} \int_0^{2\pi} \mathrm{d}\psi \int \mathrm{d}\mathbf{x} \, f(\mathbf{x}) \mathcal{H} \left\{ \delta' \left[\mathbf{n} \cdot (\mathbf{x} - \mathbf{x}_0) \right] \right\}. \end{aligned} \tag{5.8}$$

The definition of the inverse Radon transform in equation (5.8) indicates that function $f(\mathbf{x})$ (in our case the scattering potential at constant θ) may be reconstructed at any point $\mathbf{x}_0$ by summing function $F(\mathbf{n}, s)$ over all planes passing through point $\mathbf{x}_0$. Unlike the Radon transform, however, the surfaces represented in the present derivation are curvilinear (e.g., the isochrons illustrated in Figure 5.3) but these may treated as locally planar in the vicinity of point $\mathbf{x}_0$ (see *Miller et al.*, [1987]). This identification allows for the definition of a back projection operator that reconstructs the θ-dependent scattering potential, $f^q(\mathbf{x}, \theta)$, as,

$$f^q(\mathbf{x}_0, \theta) = \frac{1}{4\pi} \int \mathrm{d}\psi \, \frac{|\nabla \mathcal{T}_0^q|^2}{|\mathcal{A}^q|^2} \sum_n \mathcal{A}_n^q(\mathbf{x}_0, \mathbf{x}', \mathbf{p}_\perp^0) v_n^q(\mathbf{x}', \mathbf{p}_\perp^0, t = \mathcal{T}_0^q). \tag{5.9}$$

Using the definition of $f^q(\mathbf{x}_0, \theta)$ in equation (5.2), and recognizing that the number of measurements over variable θ yield an overdetermined linear system at model point $\mathbf{x}_0$, the angular dependence θ may be treated in a least-squares sense thus allowing for the recovery of material property perturbations, $\Delta\mathsf{m}$, as

$$\Delta\mathsf{m} = \mathsf{H}^{-1}\mathbf{g}. \tag{5.10}$$

The elements of $\mathbf{g}$ are given by,

$$g^q(\mathbf{x}_0) = \frac{1}{4\pi}\int \mathrm{d}\left|\mathbf{p}_\perp^0\right| \int \mathrm{d}\theta \int \mathrm{d}\psi \sum_k W_k^q(\theta) \frac{|\nabla \mathcal{T}_0^q|^2}{|\mathcal{A}^q|^2} \sum_n \mathcal{A}_n^q(\mathbf{x}_0, \mathbf{x}', \mathbf{p}_\perp^0) v_n^q(\mathbf{x}', \mathbf{p}_\perp^0, t = \mathcal{T}_0^q) \quad (5.11)$$

$$= \frac{1}{4\pi}\int \mathrm{d}\left|\mathbf{p}_\perp^0\right| \int \mathrm{d}\gamma \int \mathrm{d}x_1' \left|\frac{\partial(\psi,\theta)}{\partial(x_1',\gamma)}\right| \sum_k W_k^q(\theta) \frac{|\nabla \mathcal{T}_0^q|^2}{|\mathcal{A}^q|^2} \sum_n \mathcal{A}_n^q(\mathbf{x}_0, \mathbf{x}', \mathbf{p}_\perp^0) v_n^q(\mathbf{x}', \mathbf{p}_\perp^0, t = \mathcal{T}_0^q),$$

where the Jacobian transformation has been introduced in equation (5.11) to transform the integration over geometrical quantities ψ, θ (see Figure 5.3) into source, γ, and receiver, x_1', variables. The elements of the Hessian matrix H are given by,

$$H_{lq}(\mathbf{x}_0) = \int \mathrm{d}\left|\mathbf{p}_\perp^0\right| \int \mathrm{d}\theta \sum_k W_l^k(\theta, \left|\mathbf{p}_\perp^0\right|, \mathbf{x}_0)\, W_k^q(\theta, \left|\mathbf{p}_\perp^0\right|, \mathbf{x}_0). \quad (5.12)$$

The inverse problem can, accordingly, be viewed simply as a weighted diffraction stack over all sources and receivers with weights determined through analogy with the Radon transform. That is, the scattering potential, $g^q(\mathbf{x}_0)$, defined in equation (5.11) is constructed at any given model point $\mathbf{x}_0$ by an event-by-event weighted summation of energy along travel time curves corresponding to the arrival time of the scattered at the surface from point $\mathbf{x}_0$. This function is then employed in equation (5.10) to recover the perturbations in material properties, $\Delta\mathsf{m}$, through a trivial 3×3 matrix multiplication.

5.2 Research Goal

The objective of Part II of this thesis is to investigate the potential of this inversion methodology through a variety of numerical simulations. Specifically, its main contribution is to evaluate the performance of the algorithm in a controlled, idealized environment and to provide insight into limitations and potential problems that may arise during inversion of field data (i.e., *Rondenay et al.*, [2000]). To this end, synthetic 2-D simulations have been designed which comprise interaction of upward-propagating plane waves with a model lithospheric suture zone. This class of

structure is a typical target in lithospheric-scale geophysical surveys (e.g., *Calvert et al.*, [1995]) and one which produces a response sufficiently complex that conventional teleseismic processing (i.e., radial component receiver functions) approaches may yield results which are not straightforward to interpret. Details of the subduction zone model used in numerical simulations, including the generation of synthetic data from this model and its subsequent preprocessing, are discussed in Chapter 6. In the following chapter, the synthetic data set is utilized in a series of inversions to identify the importance of the roles that various parameters play in the recovery of structure.

5.3 Author's Contribution

The research contained in Part II of this thesis has been accepted pending minor revisions in the *Journal of Geophysical Research* as the second installment of a tri-partite series (i.e., *Paper I*; *Shragge et al.*, [2000], hereafter referred to as *Paper II*; and *Rondenay et al.*, [2000], hereafter referred to as *Paper III*) that develops, tests, and applies this new teleseismic imaging technique. This material has also been presented in abbreviated form in a series of posters and oral communications at scientific meetings. Chapter 5 comprises a summation of theory outlined in *Paper I*, and is similar to the overview presented in the thesis of my co-author Stéphane Rondenay [*Rondenay*, 2000]. Chapters 6 and 7 are based in major part on *Paper II*. The research in all of *Papers I, II,* and *III* was conducted in close collaboration between myself, Michael Bostock, and Stéphane Rondenay. While the principal author of each paper was responsible for the main contribution, co-authors were actively involved in most aspects of the research. In particular, I assisted in the writing of the computer code dealing with inversion of multi-event in-plane sources, generated and developed preprocessing procedures for synthetic data, and devised, conducted, and analysized results from numerical simulations.

Chapter 6

Generation of synthetic data

Chapter overview: This chapter begins with a brief summary of documented lithospheric sutures as imaged in seismic reflection surveys and which have motivated the design of our idealized numerical model. The forward modelling of teleseismic *P*-wave propagation through this lithospheric model using a pseudo-spectral numerical method is then described, and followed by an outline of the preprocessing required to prepare raw displacement seismograms for inversion.

6.1 Lithospheric Suture Model

Lithospheric suture zones are the signatures of collisions between continents which generally culminate extended periods of ocean-continent subduction. As such, they represent one of the more complex structures likely to be encountered in studies of the continental lithosphere. The evolution of lithospheric suture zones arising from smaller-scale, convergent boundaries (i.e., less than $\sim$150 km in horizontal extent) has been investigated using 2-D, finite-element modelling [*Beaumont and Quinlan*, 1994; *Fullsack*, 1995] for a range of crustal models differing in geothermal gradient, composition and structural geometry. A key factor in the development of lithospheric sutures is the location of the brittle-ductile transition within the crustal column which divides the crust rheologically into an overlying viscoplastic layer and an underlying, more competent lithospheric mantle (e.g., *Fullsack*, [1995]). The lithospheric detachment point associated with

this boundary governs the location where lithospheric materials partition into obducting and subducting segments. In hotter thermal regimes where the brittle-ductile transition occurs nearer to surface, there is a corresponding increase in the volume of lithospheric material subducted into the mantle. Thus, the thickness of a subducting segment is thought to be strongly dependent on the vertical extent of crustal column below the brittle-ductile transition. The situations modelled by *Beaumont and Quinlan* [1994] for which transitions occurred in the mid-crust resulted in subducted segment thicknesses between 10-20 km.

Suture zones have been documented in a number of high-resolution seismic reflection profiles traversing both Phanerozoic and Precambrian orogens (e.g., *Pfiffner et al.*, [1990]; *Calvert et al.*, [1995]; *Cook et al.*, [1998]). These studies provide the principal constraints on the deep-seated geometry of suture zones through: i) reflections from the Moho which often indicate crustal thickening followed by abrupt thinning; ii) the presence of dipping mantle reflections that document penetration of subducted crustal segments, in some cases, to depths of $\sim$100 km or more (e.g., *Cook et al.*, [1998]); and iii) reflection amplitudes which suggest that subducted material has undergone dehydration reactions (e.g., *Calvert et al.*, [1995]). Although seismic reflection profiles provide the most detailed views of lithospheric sutures, they are limited in at least two respects. First, the use of anthropogenic sources limits depth penetration to uppermost mantle levels. Second, the narrow and relatively high signal bandwidth of conventional seismic sources often precludes accurate determination of signal polarity and, hence, sign of impedance contrasts. Densely sampled teleseismic profiles would not suffer from these limitations and, accordingly, could provide important complementary information on complex lithospheric structures.

Our idealized lithospheric suture model, shown in Figure 6.1 and loosely based on the aforementioned studies, is defined over a 360×120 km^2 section and consists of three materials with differing elastic properties. A low-velocity crustal layer overlies a faster upper mantle (see Table

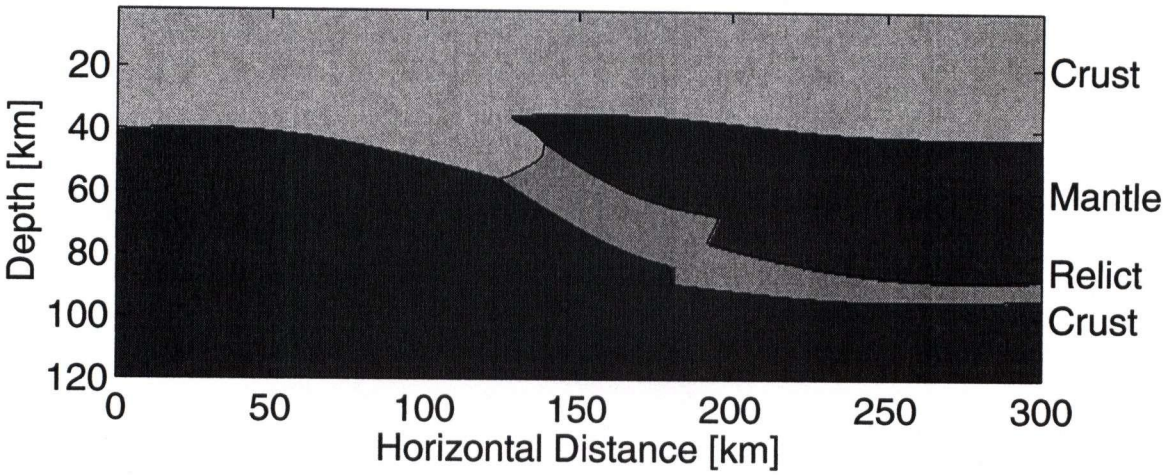

Figure 6.1: Idealized lithospheric subduction-suture model. Velocities and densities of each material are given in Table 6.1.

6.1 for model velocities and densities). At the location of the suture, crustal material from the lithospheric block to the left bifurcates, with the lower segment descending into the mantle. At a depth of ~40 km, it converts to velocities and density higher then the surrounding mantle (note the proportionally greater increase in *S*-velocity) and thereafter folds and thins to the right of the model. Heterogeneity comprises both dipping, locally planar interfaces (i.e., the slowly varying Moho, subducting segments) from which specular conversions and reflections are expected, and sharper, angular discontinuities (i.e., mantle wedge, slab fold) which will produce more complex scattering, loosely referred to here as diffraction. Thus, the model should afford a reasonable test of the algorithm's ability to image a range of structural complexity.

6.2 Generation of Synthetics

Several data sets of two-component seismograms were computed through the lithospheric model described above using a 2-D, elastic pseudo-spectral code [*Kosloff et al.*, 1990]. The model was

Table 6.1: Lithospheric model parameters.

Parameter	P-wave velocity (km s^{-1})	S-wave velocity (km s^{-1})	Density (g cm^{-3})
Crust	6.2	3.6	2.8
Mantle	8.0	4.5	3.2
Relict Crust	8.1	4.9	3.3

discretized at 0.6 km intervals in both directions which, given the minimum velocity in our model (3.6 km s^{-1}), allows for frequencies up to 4.0 Hz to be accurately modelled. This value corresponds approximately to the upper frequency limit of *P*-wave seismograms from teleseismic events.

The data sets comprise a suite of plane *P*-waves interacting with the suture model at a range of incident horizontal slownesses, p_1^0 = [0.05, -0.05, 0.06, -0.06, 0.07, -0.07] s km^{-1}. A Gaussian waveform, e^{-18t^2} (t measured in seconds), was chosen to approximate the incident delta-function pulse (i.e., Green's function) required in the inverse formulation. The planar wavefront is a close approximation to that of a teleseismic *P*-wavefront predicted from spherical Earth models where the change in horizontal slowness over a 300 km interval at the Earth's surface will not generally exceed a few percent. The output seismogram sections consist of 600 traces recorded at the free surface. These sections are subsequently desampled by a factor of five to yield data sections of 120 traces sampled at 3 km intervals as input for inversion. To allow incorporation of the free-surface back-scattered response, the duration spanned by individual records is approximately 50 s after the direct arrival.

6.3 Preprocessing and Synthetic Results

Implementation of the method in *Paper I* requires that the so-called scattered wavefield $\Delta\mathbf{u}$ is effectively isolated (see equations (24-25,43-45), *Paper I*). The technique employed here is that of *BR* who detail a procedure through which the incident wavefield $\mathbf{u}^0$ (i.e., the *P*-wavefield which would propagate in a smoothly varying 1-D reference medium) is approximately removed from a multichannel seismogram section to yield an estimate of the scattered wavefield. The method may be summarized as follows: i) the raw data sections, $\mathbf{u}$=$[u_1, u_2]$, are transformed into upgoing *P*- and *S*-wavefield sections, $\mathbf{w}$=$[P, SV]$, via the free-surface transfer matrix [*Kennett*, 1991]; ii) multi-channel cross-correlation [*VanDecar and Crosson*, 1990] is applied to a window about the direct (high-pass filtered) *P*-arrival to allow optimal alignment of the wavefield sections; iii) the aligned *P*-section is decomposed into its principal components through diagonalization of the zero-lag, cross-correlation matrix; iv) the first (or first few) principal component(s) are identified with the source time function of the incident wavefield while the remaining principal components (or some selection thereof) are associated with the scattered wavefield; v) the scattered displacement sections are reconstituted from the *P*- and *S*- wavefield sections using the inverse free-surface transfer matrix; vi) in practice, individual source time function estimates (as obtained by the above procedure) are then deconvolved from the scattered displacement to yield the scattered wavefield $\Delta\mathbf{u}$; however, this step is not employed here as the Gaussian source-time function is essentially a low-pass filtered approximation of the delta-function-like impulse-response required by theory. The final stage of preprocessing entails a convolution of $\Delta\mathbf{u}$ with a filter whose frequency domain representation is $F(\omega) = -\mathrm{i}\,\mathrm{sgn}(\omega)/\sqrt{-\mathrm{i}\omega}$, to produce a new time series $\mathbf{v}$ (equation (5.4)) as required by the 2-D plane-wave migration scheme to directly image jumps in elastic properties across discontinuities. Each trace is then subjected to a bandpass Butterworth

filter between 0.1 Hz and 4.0 Hz to approximate the typical frequency bandwidth from a deep teleseismic event.

Two-component, processed (but prior to application of $F(\omega)$) scattered displacement waveforms (i.e., $\Delta\mathbf{u}$) for incident horizontal slownesses, p_1^0, of -0.07 and 0.07 s km^{-1} are shown in Figures 6.2a-d. Individual scattered phases apparent in Figures 6.2a-d include both forward-scattered waves (q=1,2; equations (24,25) in *Paper I*), and back-scattered modes (q=3,4,5,6,7; equations (24,25,43-45) in *Paper I*) afforded through free-surface reflection of the incident up-going *P*-wavefield into downgoing *P*- and *S*-waves. To summarize (see also Figure 5.2) q=1,3 represent *P-P* scattering; q=2,4 represent *P-S* scattering; q=5 represents *S-P* scattering; and q=6,7 represent different modes of *S-S* scattering (only one *S-S* scattering mode, q=6, is required for the in-plane, 2-D geometry of the present problem). The horizontal component response for right incidence, Figure 6.2a, is dominated by a *P-S* conversion (q=2) from the Moho arriving at $\sim$5 s and a *P-P* diffraction (q=1) centered at 100 km with apex at $\sim$ 0 s. Subsequent arrivals are most obvious on seismograms to the right of the suture: i) a combination of *P-S* (q=2) scattering originating from either side of the subducted crustal segment at $\sim$10-11 s; ii) a back-scattered *P-S* conversion (q=4) from the Moho at $\sim$17 s; and iii) a *S-S* reflection (q=6) from the Moho at $\sim$22 s. The vertical component, Figure 6.2b, emphasizes two further arrivals: i) a *P-P* phase reflection (q=4) from the Moho at $\sim$11 s; and ii) a weaker *S-P* conversion (q=5) from the Moho at $\sim$17 s. These phases represent the dominant contributions to scattering; several other "kinematic analogues" involving interaction with the free surface may also be identified but these represent effectively second order contributions.

Figures 6.2c,d present the corresponding displacement components for a plane wave incident from the left. The amplitudes of converted phases (q=2,4,5) from the near-planar horizons are diminished with respect to Figures 6.2a,b because the specular angles are closer to perpendicular

(and hence the conversion coefficients closer to zero) while diffracted signals from the suture are more pronounced. A series of diffractions, all centered near ~150 km in offset, are apparent: i) a *P-P* diffraction (q=1) with apex at ~0 s (Figure 6.2d); ii) two *P-S* diffractions (q=2) with apices at ~5 s and ~7 s (Figure 6.2c); iii) a *P-P* diffraction (q=3) with apex at ~10 s (Figure 6.2d); and iv) a *S-P* diffraction (q=5) with apex at ~16 s (Figure 6.2d).

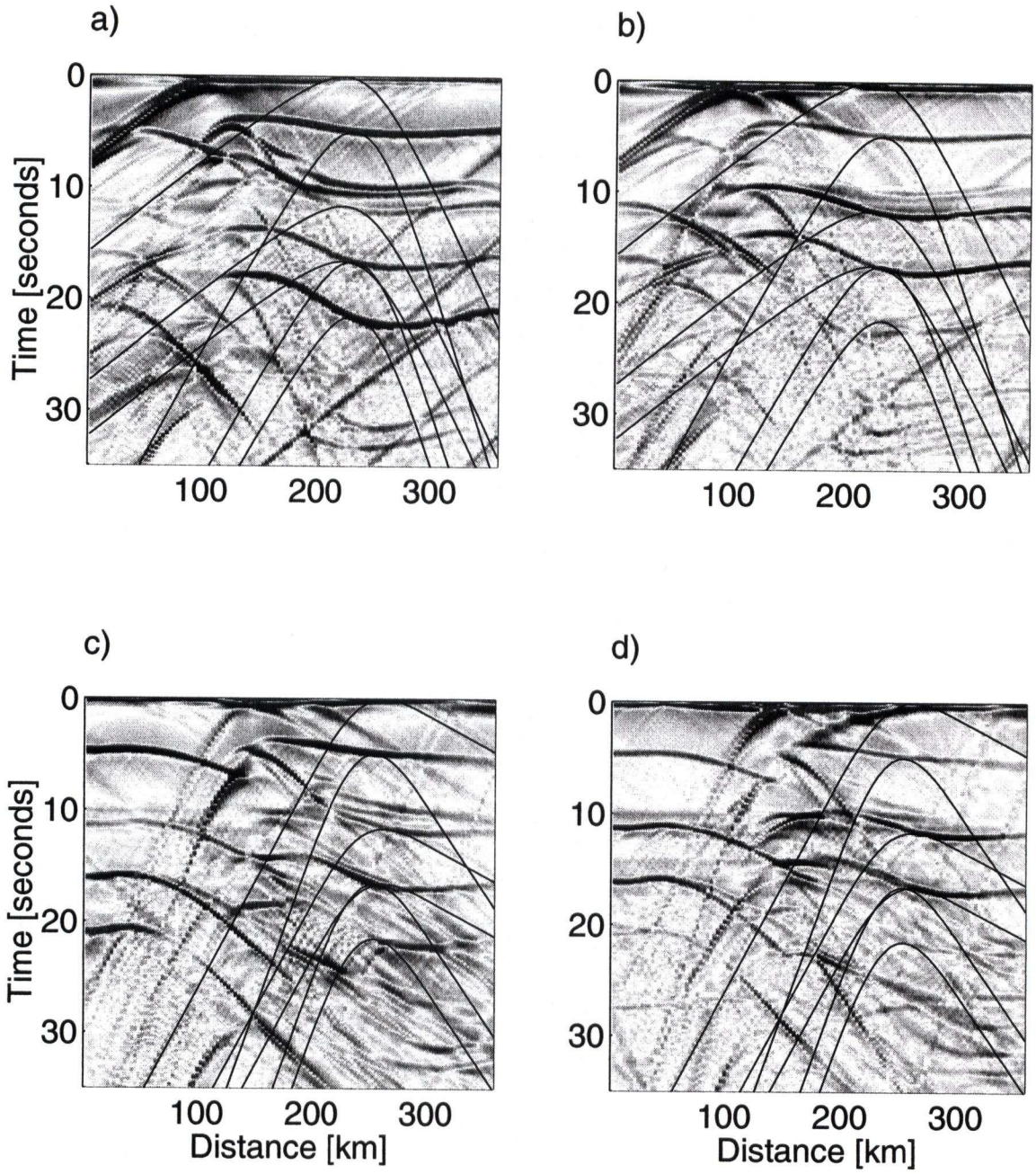

Figure 6.2: Preprocessed (but prior to filtering by $F(\omega)$) synthetic data sections generated for the idealized lithospheric model in Figure 6.1. a) Δu_1 and b) Δu_3 components for an incident plane wave with horizontal slowness p_1^0=-0.07 s km^{-1}; c) Δu_1 and d) Δu_3 components for an incident plane wave with horizontal slowness p_1^0=0.07 s km^{-1}. Examples of travel time curves, $\mathcal{T}^q$ (q=1,2,3,4,5,6 in order of increasing time) are superposed for model point $\mathbf{x}$=[240 km, 40 km].

Chapter 7

Migration Simulations

Chapter overview: The inversion methodology described in Chapter 5 is applied here to the synthetic data sets in a series of investigations to assess its potential and limitations. Simplifications to the migration/inversion theory permitted by the 2-D, in-plane propagation of the present experiment are discussed, followed by a brief summary of travel time calculations, the 1-D earth model chosen as reference, and the parameterization of inversion results. An examination of the numerical simulations begins with the imaging potential of forward-scattered modes from single events. Subsequently, all forward-scattered *P-S* responses are combined in a single inversion to gauge the improvements resulting from enhanced source coverage. The remaining free surface reflected modes are then investigated to compare differences in resolution between forward- and back-scattered interactions. Following this, a majority of scattering interactions from all events are combined in a single inversion to further improve the reconstruction of subsurface discontinuous structure. This chapter concludes with a brief analysis of the degradation accruing from the introduction of noise and reduced station sampling.

7.1 Simplifications to Migration Theory

The intent of this section is to summarize several key results from the overview presented in Chapter 5 and amend them slightly to forms appropriate for the in-plane geometry of the present problem. The most obvious simplification involves the restriction of all vector quantities (e.g., filtered,

scattered displacement $\mathbf{v}$, incident slowness $\mathbf{p}^0$, scattered slowness $\mathbf{p}^S$) to the x_1,x_3 plane. Accordingly, equation (5.11) is rewritten as,

$$g^q(\mathbf{x}) = \int \mathrm{d}p_1^0 \int \mathrm{d}x_1' \left| \frac{\partial(\psi,\theta)}{\partial(x_1',p_1^0)} \right| \sum_l W_l^q(x_1',p_1^0,\mathbf{x}) \frac{|\nabla \mathcal{T}^q|^2}{|\mathcal{A}^q|^2} \sum_n \mathcal{A}_n^q(\mathbf{x},\mathbf{x}') v_n^q(\mathbf{x}',p_1^0,t=\mathcal{T}^q), \quad (7.1)$$

where quantities are defined as in Chapter 5. Note that the integration over sources is now cast in terms of the Cartesian horizontal slowness, p_1^0, rather then its absolute value, $|\mathbf{p}_\perp^0| = \sqrt{(p_1^0)^2 + (p_2)^2}$, cf. Chapter 5. The Jacobian change of variables in equation (7.1) is altered by the loss of one degree of freedom in the data variables, and, accordingly equation (73) in *Paper I* reduces to,

$$\left| \frac{\partial(\psi,\theta)}{\partial(x_1',p_1^0)} \right| = \left| \frac{\cos\phi}{(J^S)^2} \frac{\alpha}{\sqrt{1-(p_1^0)^2\alpha^2}} \right|, \quad (7.2)$$

for a *P-S* interaction where ϕ is the surface take-off angle of the scattered ray and J^S is the *S*-wave geometrical spreading function between scatter point, $\mathbf{x}$, and receiver location, $\mathbf{x}'$. The Jacobian is modified from equation (7.2) when considering other scattering interactions by: i) a replacement of J^P for J^S for modes q=1,3,5; and ii) a substitution of β for α for modes q=5,6. With these modifications, the material property perturbations at any particular scatter point are similarly retrieved as,

$$\Delta \mathbf{m} = \mathsf{H}^{-1}\mathbf{g}, \quad (7.3)$$

where the three elements of gradient, $\mathbf{g}$, are obtained from equation (7.1), and the Hessian, H, following equation (5.12), is given by,

$$H_{lq}(\mathbf{x}) = \int \mathrm{d}p_1^0 \int \mathrm{d}\theta \sum_k W_l^k(\theta,p_1^0,\mathbf{x}) W_k^q(\theta,p_1^0,\mathbf{x}), \quad (7.4)$$

where the dependence of W_l^q on θ, p_1^0, and $\mathbf{x}$ is explicitly identified.

7.2 Calculation of Travel Times

Equation (7.1) is akin to the diffraction stack of classical migration and defines the potential function $g^q(\mathbf{x})$, at any model point $\mathbf{x}$, as a weighted summation over all receivers and events of the data along predicted travel time curves for the particular mode interaction, q, as determined for the smoothly varying, 1-D reference medium (see section 7.3). Examples of travel time curves for the different scattering modes are superposed on Figures 6.2a-d for a model point $\mathbf{x}$=[240 km,40 km] at Moho depth. The scattered wave travel times, $\mathcal{T}^q$, normalized with respect to the direct *P*-arrival, are easily calculated for a 1-D reference model. For a direct *P-S* conversion (q=2) travel time $\mathcal{T}^{(2)}$ is given by,

$$\mathcal{T}^{(2)}(\mathbf{x}, x_1', p_1^0) = \int_0^{x_3} \frac{\mathrm{d}y_3}{\beta(y_3)\sqrt{1-\beta^2(y_3)(p_1^S)^2}} - p_1^0(x_1' - x_1) \tag{7.5}$$

$$- \int_0^{x_3} \frac{\mathrm{d}y_3}{\alpha(y_3)} \sqrt{1-\alpha^2(y_3)(p_1^0)^2}, \tag{7.6}$$

where p_1^S is the horizontal slowness of the ray travelling between scatter point $\mathbf{x}$ and receiver $\mathbf{x}'$. For a direct *P-P* interaction (q=1), p_1^P (horizontal slowness of the scattered *P*-wave) and α are substituted for p_1^S and β, respectively.

When calculating the expected arrival times for back-scattered waves, both the extra time incurred by a wave traveling to surface and returning to the scatterer point, and for the possibility of *P-S* conversion at the free surface must be taken into account. Thus, the expected travel time for, e.g., a back-scattered *P-P* (q=3) interaction is

$$\mathcal{T}^{(3)}(\mathbf{x}, x_1', p_1^0) = \int_0^{x_3} \frac{\mathrm{d}y_3}{\alpha(y_3)\sqrt{1-\alpha^2(y_3)(p_1^P)^2}} - p_1^0(x_1' - x_1) \tag{7.7}$$

$$+ \int_0^{x_3} \frac{\mathrm{d}y_3}{\alpha(y_3)} \sqrt{1-\alpha^2(y_3)(p_1^0)^2}. \tag{7.8}$$

Travel times for other phases are calculated with slight modification: i) *P-S* scattering (q=4) requires substitutions of p_1^S and β for p_1^P and α in the first term; ii) for *S-P* scattering (q=5), α is

replaced by β in the third term; and iii) *S-S* scattering (q=6) requires all three of the substitutions in i) and ii).

Two further points are worth noting. First, the travel times of scattered modes which share similar polarizations at the receiver differ only by static time shifts for the 1-D reference model. Second, asymmetries about the scatter point exist in the travel time moveout with distance which result from the p_1^0 dependence in equations (7.5) and (7.6) as manifest by tilt in the hyperbolae in Figures 6.2a-d. In particular, the expected travel time moveout for, e.g., a forward-scattered *P-S* interaction in a 1-D medium is noted to be,

$$\frac{\partial T^{(2)}}{\partial x_1'}(\mathbf{x}, x_1', p_1^0) = -p_1^0 + \frac{\partial p_1^S}{\partial x_1'} \int_0^{x_3} \mathrm{d}y_3 \frac{\beta(y_3) p_1^S}{[1 - \beta^2(y_3)(p_1^S)^2]^{\frac{3}{2}}}. \tag{7.9}$$

7.3 Reference Model and Parameterization

In the sections that follow, a 1-D reference model consisting of a 40 km thick crust overlying an upper mantle half-space is utilized. Velocities and densities of these two reference materials are identical to the crustal and mantle properties specified in the first two rows of Table 6.1. In addition, inversion for only $\Delta\alpha/\alpha$ and $\Delta\beta/\beta$, the two most linearly independent parameters in the case of forward-scattering (e.g., *BR*), is considered since the third parameter (i.e., $\Delta\rho/\rho$) remains effectively indeterminate for surface receiver arrays. In situations where back-scattering is represented, this is recognized as not the best choice of parameter combination (see, e.g., *Forgues and Lambaré*, [1997]). However, *Forgues and Lambaré* [1997] demonstrate that any choice of parameterization may be simply recovered through matrix multiplications after inversion. Thus, for simplicity, all inversion results are presented in terms of the physically meaningful, though not always optimal, velocity perturbations.

7.4 Receiver Function Image of Synthetic Data

Before proceeding to detail individual experiments, it is desirable to present a basis for comparison between our inversion methodology and conventional teleseismic processing. A receiver-function image (e.g., *Langston*, [1979]) constructed via least-squares simultaneous deconvolution (e.g., *Gurrola et al.*, [1995]) of individual *S*-wave traces by corresponding *P*-wave traces (as determined in step 1 of the pre-processing sequence) from all six events is shown in Figure 7.1. Well defined *P*-to-*S* conversions from the Moho and subducted crust are apparent to the left and right of the suture. However, traces to the left side of the section and near the suture at offsets of ~120 km are corrupted by strong forward-scattered *P-P* and *P-S* diffraction energy (cf. data

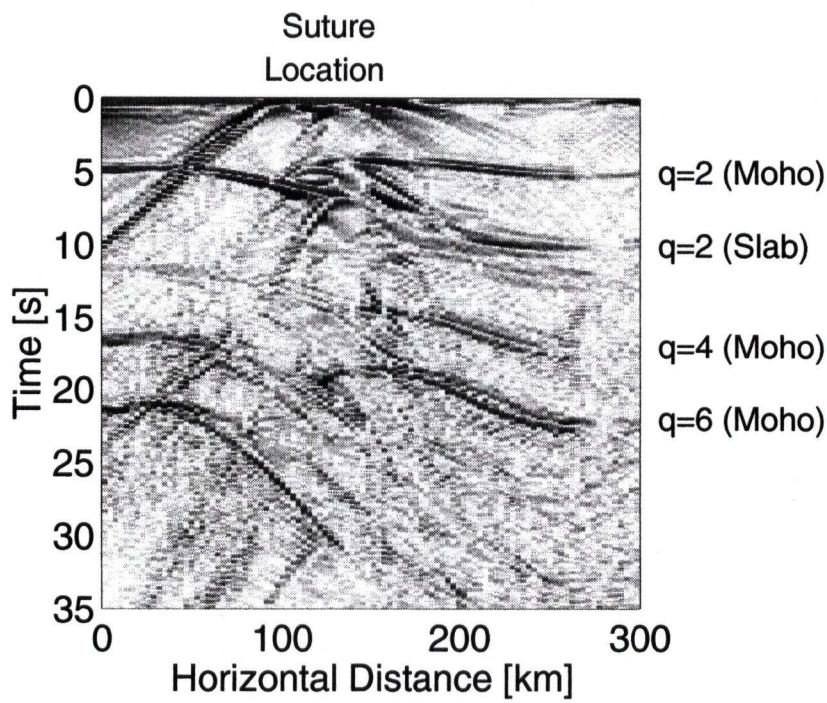

Figure 7.1: Least squares receiver function image constructed through simultaneous deconvolution of individual *S*-wave traces by corresponding *P*-wave traces for all six suites of seismograms.

sections in Figures 6.2). Free-surface multiples corresponding to interactions q=3,4,6 are evident at times later than 10 s, and may be potentially misinterpreted as deeper structure. A formal, multiple mode inversion is expected to significantly reduce these contaminating artifacts, and allow for an improved imaging of more complex structure.

7.5 Experiment I - Single Event Inversion of Forward-Scattering Modes

To examine the bias resulting from source direction, forward-scattering modes q=1,2 are inverted separately for two events with positive (p_1^0=0.07 s km^{-1}) and negative (p_1^0=-0.07 s km^{-1}) horizontal slowness (Figures 7.2 and 7.3, respectively). Because of the limited sampling afforded by a single event, recovery is restricted to a single material parameter for both modes using the Jacobian, $|\partial\psi/\partial x_1'|$, in equation (74) of *Paper I*. In particular, perturbations $\Delta\alpha/\alpha$ for q=1 and $\Delta\beta/\beta$ for q=2 are considered as optimal choices for forward scattering. Furthermore, due to the strong amplitudes evident in Figure 7.1 between zero and four seconds, a cosine taper has been applied to the beginning of all traces employed in this and the following experiments. The *P*-velocity perturbations reconstructed from the forward-scattered *P*-*P* (q=1) interaction are presented in Figure 7.2a. Vertical streaking about the suture zone with the correct general polarity is observed though little focussing of energy is achieved. *S*-velocity perturbations recovered by the direct *P*-*S* (q=2) interaction (Figure 7.2b) afford a much better delineation of the normal-relict crust boundary. Note that apart from this boundary, little of the remaining, more planar components of structure is reconstructed.

Figures 7.3a,b present the same parameter and mode interaction combinations as Figures 7.2a,b, but now for an incident wave with slowness -0.07 s km^{-1}. Figure 7.3a shows increased streaking about the suture zone, relative to Figure 7.2a, and a correlation with actual structure

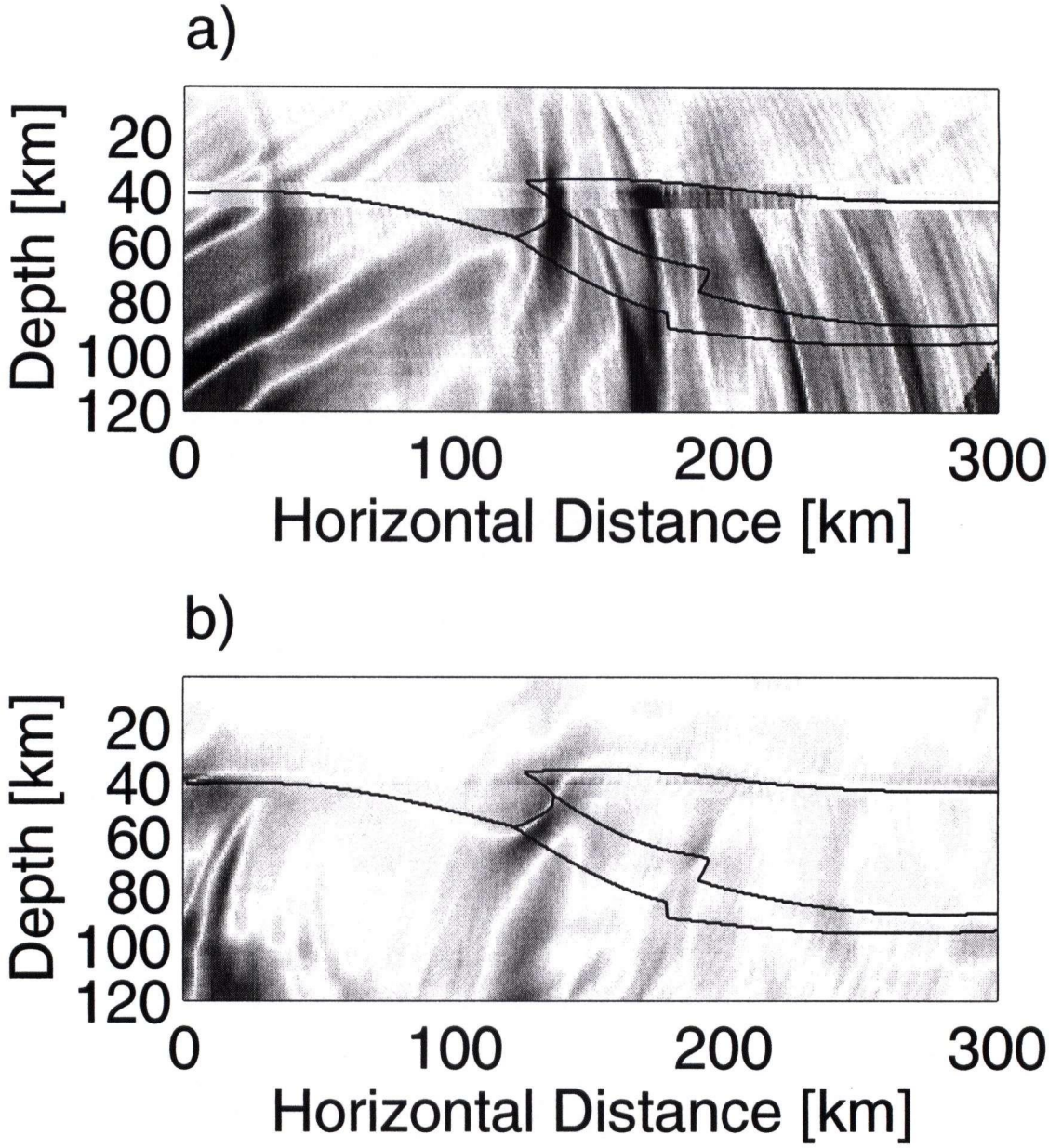

Figure 7.2: Reconstructed velocity perturbations from inversion of forward-scattered modes for a left-incident plane wavefield (p_1^0=0.07 s km^{-1}). a) $\Delta\alpha/\alpha$ from q=1; b) $\Delta\beta/\beta$ from q=2.

that is poorer still. Unlike Figure 7.2b, the S-velocity image in Figure 7.3b reconstructs the relict crust-mantle boundaries (though displaced upwards from their true locations), but identifies little contrast with adjacent normal crust. The Moho is now more prominent, though its location is

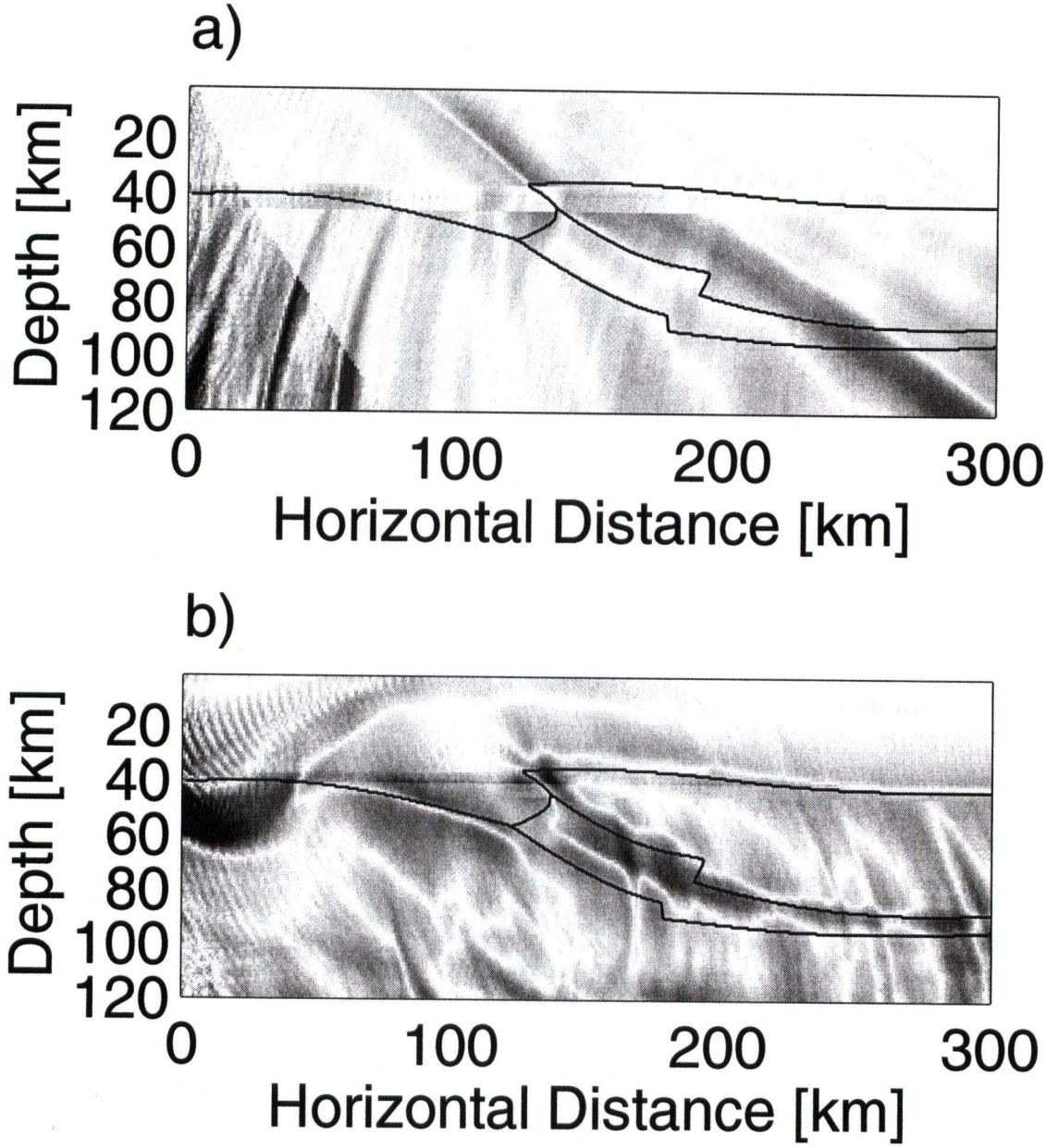

Figure 7.3: Reconstructed velocity perturbations from inversion of forward-scattered modes for a right-incident plane wavefield (p_1^0=-0.07 s km^{-1}). a) $\Delta\alpha/\alpha$ from q=1; b) $\Delta\beta/\beta$ from q=2.

slightly displaced from the known lithospheric model. The mislocation of structure is related to the inadequacy of the reference velocity model in correctly predicting the travel times of scattered phases. Where Moho depths are less then 40 km, there is a corresponding "pull up" of underlying

structure, while the converse is true in areas where the Moho exceeds 40 km.

The present experiment serves to illustrate several of the shortcomings inherent in single-mode inversions in general, and forward-scattering inversions in particular. Of specific note is the poor recovery of structure in the forward-scattered *P-P* images (Figures 7.2a and 7.3a). The origin of this lack of sensitivity can be traced directly to the factor $|\nabla \mathcal{T}^q|^2$ that appears in equation (7.1) and weights the diffraction stack according to the sensitivity of total travel time to scatterer location. For q=1 in the strictly forward-scattering direction (θ= 180°), the sensitivity is zero, as discussed extensively by *Marquering et al.* [1999], and remains relatively small for a range of angles about the forward direction. A consequence of this behaviour is that considerable tradeoff exists between the lateral extent of the scattering body and its depth in near-forward directions. This effect is manifest in the diffuse appearance of reconstructed anomalies in Figures 7.2a and 7.3a.

A second issue worth noting is the contrasting recovery of structure for events with differing horizontal slowness. In general, the successful reconstruction of a material property perturbation is dependent upon the strength of the associated scattered response. In the case of extended, quasi-planar discontinuities separating gently varying media, this scattered response will be most pronounced in directions corresponding to the specular angle of interaction. For *P*-to-*S* conversions (q=4), however, the effect of conversion coefficients, which tend to zero as the specular angle approaches 0°, must also be considered (i.e., normal incidence). In this case, the incident wavefield has little sensitivity to structure since no *P-S* scattering results. Consequently, the structure can be regarded as falling within the null space of the problem and will not be recovered within the inversion.

These effects are well illustrated in Figures 7.2b and 7.3b. In the case of left incidence (Figure 6.2c,d), *P-S* (q=2) scattering from the subhorizontal boundaries is weak since the incoming wavefield is incident at near-normal angles. The sole exception is the short boundary segment between normal and relict crust which is sufficiently limited and oblique to generate strong diffractions. Consequently, only the latter feature is well resolved in the inversion Figure 7.2b. In contrast, illumination of the lithospheric section by a plane wave from the right (Figure 6.2a,b) produces stronger *P-S* conversions from the near-planar structures as they are oriented at more oblique angles to the incident wave. Accordingly, Figure 7.3b documents an improved reconstruction of the Moho and the lateral extent of subducted relict crust.

7.6 Experiment II - Multiple Event Inversion of Forward-Scattering Modes

The present section investigates the effect of simultaneous inversion of multiple events on the reconstruction of material properties. In this experiment and those that follow, the Jacobian change of variables in equation (7.2) is employed as a range of incident slowness p_1^0 is now sampled. The reconstructed *P*- and *S*-velocity images from the inversion of all six forward-scattered *P-P* and *P-S* interactions are presented in Figures 7.4a,b, respectively. As might be expected, the image in Figure 7.4b combines the structural features imaged separately in Figures 7.2b and 7.3b. In particular, all of the boundaries which define the suture are now well resolved, and Moho velocity perturbations are retrieved at laterally coherent levels along the entire breadth of the array. However, the amplitude of the reconstructed Moho discontinuity is underestimated relative to the short wavelength suture. This is, in part, a consequence of the volume-scattering formulation as is discussed further in the following section. It is also worth noting that some contamination from scattered *P-P* (q=1) enters the image at shallow crustal levels.

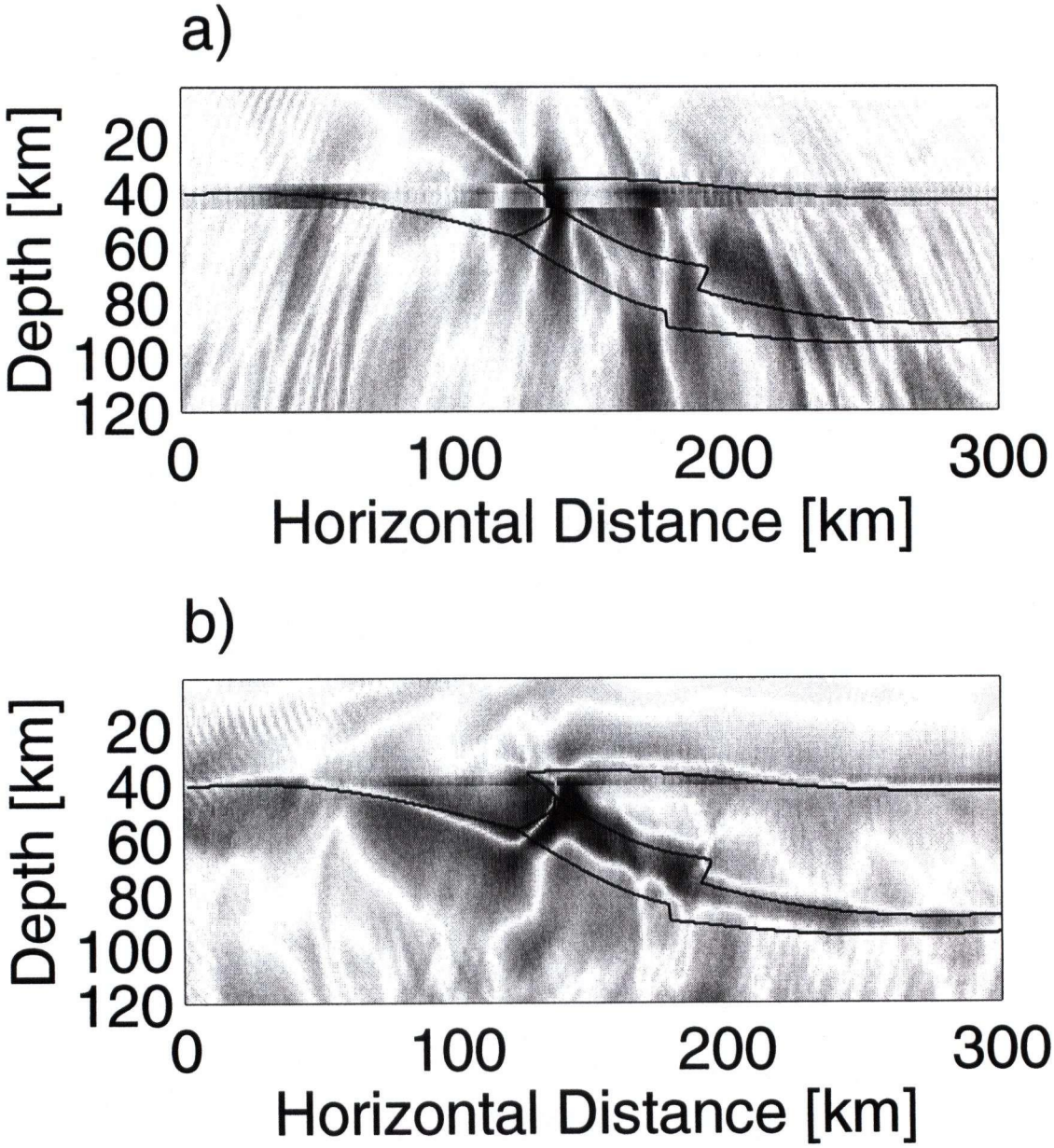

Figure 7.4: Reconstructed velocity perturbations from inversion of forward-scattered modes of all six incident plane wavefields. a) $\Delta\alpha/\alpha$ from q=1; b) $\Delta\beta/\beta$ from q=2.

Figure 7.4a documents little improvement over Figures 7.2a and 7.3a in the recovery of

discontinuous structure. In contrast with Figure 7.4b, recovered perturbations show poor correlation with the true structure. This result is thought to be due to a combination of relative insensitivity of the forward-scattered *P-P* mode to structural location and a distortion of the actual scattered *P*-wavefield incurred during preprocessing. Accordingly, this mode will not be employed in further inversions.

7.7 Experiment III - Multiple Event, Back-Scattered Mode Inversion

In this section, the inversion procedure is applied to back-scattered modes q=3,4,5,6 (Figures 7.5a-d) from all six incident wavefields. Figure 7.5a presents the reconstructed *P*-velocity perturbations for the *P-P* (q=3) reflection. In this image, the Moho and normal-relict crustal boundary

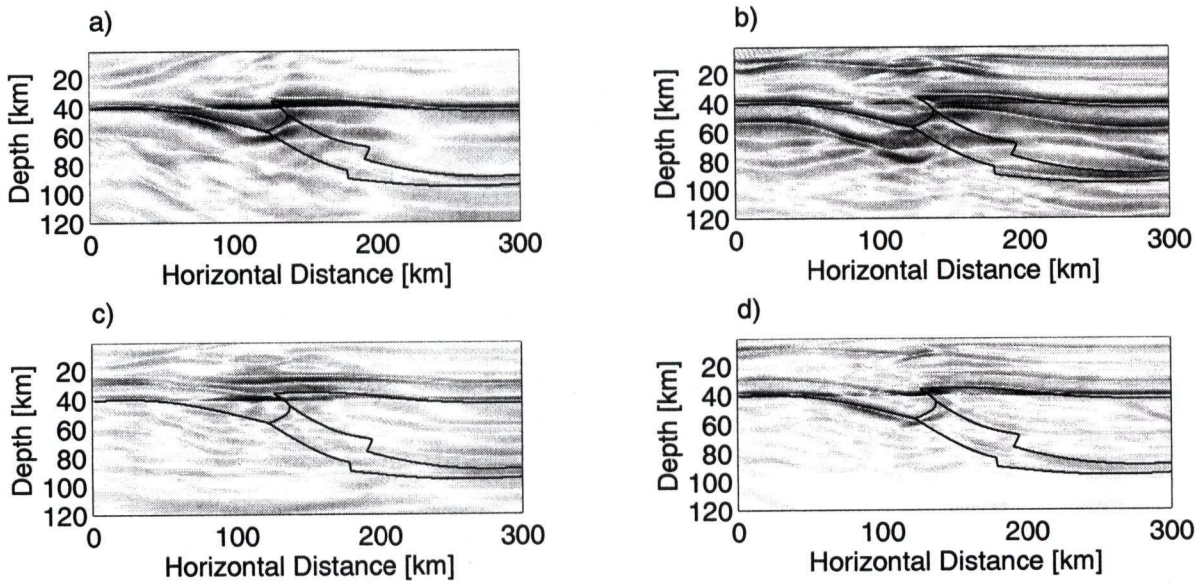

Figure 7.5: Reconstructed velocity perturbations from inversion of individual back-scattered modes for all six incident plane wavefields. a) $\Delta\alpha/\alpha$ from q=3; b) $\Delta\beta/\beta$ from q=4; c) $\Delta\beta/\beta$ from q=5; d) $\Delta\beta/\beta$ from q=6.

are accurately delineated with locations that correspond well with the actual model. In particular, the spatial localization and placement of these discontinuities is enhanced relative to that of the forward-scattering inverisons. This improvement is directly attributable to the increased sensitivity of back-scattered travel time variations to scatterer location as represented by $|\nabla T^q|^2$ in equation (7.1) and discussed in *Paper I*. Figure 7.5b presents the *S*-velocity perturbations recovered from the *P-S* (q=4) reflection. The Moho is once more well defined and is less smeared near the suture zone than in Figure 7.5a. The two discontinuous interfaces of the relict crust are also apparent and indicate the presence of a high velocity anomaly. Later arriving energy from the *S-S* (q=6) reflection contaminates the image at depths of ~60 km. *S*-velocity perturbations retrieved from the *S-P* (q=5) reflection are shown in Figure 7.5c. The strongest anomaly is located at mid-lower crustal depths, and indicates that the image is strongly contaminated by the earlier and stronger *P-P* (q=3) reflections. *S*-velocity perturbations retrieved by the *S-S* (q=6) interaction (Figure 7.5d) document a good recovery of the Moho and suture. Earlier *P-S* energy is erroneously mapped to depths near ~30 km. In general, back-scattered modes are observed to effectively resolve laterally discontinuous structure, though artifacts caused by the mis-imaging of interfering phases are more prevalent than in Figure 7.4.

An assumption inherent in the methodology is that individual scattering modes have been isolated prior to data input. In practice, this assumption can only be realized insofar as scattering modes ending as *P*- or *S*-waves can be separated on the basis of approximately orthogonal polarizations. Therefore, an obvious complication is the degree to which single mode reconstructions are contaminated by energy from other scattering interactions of similar wavetype. For example, over the range of horizontal slowness utilized in these investigations, the free-surface corrected amplitudes of *S-S* reflections from the Moho are only slightly larger (~30%) than those for *P-S* reflections. Since these phases possess similar amplitudes, both yield accurate estimates, relative

to each other, of the jumps in material properties across the Moho. However, each phase also contributes to phantom structure in the other image. This situation also exists for *P*-waves, though, in this case the amplitudes of *P-P* reflections outweigh those of *S-P* by a factor of ~4. As a result, the back-scattered *S-P* interaction is far less effective in the imaging process. As shown in the following section, the problem of mode inseparability is partially offset through simultaneous inversion of all modes; however, it is important for confident interpretation that individual mode inversions are examined at this stage for features common to all images.

Although the appearance of forward and back-scattered phases on seismograms (e.g., *P-S* interactions q=2,4 in Figure 6.2) are quite similar (aside from the static time shifts), they produce rather different images. In particular, the jump across the Moho in the forward-scattering reconstruction is noted to be rather more diffuse relative to shorter wavelength structure than for back scattered modes. An understanding of this behaviour requires an examination of the contributions from different factors ($W_l^q(\theta)$, $|\nabla \mathcal{T}^q|^2$, $|\partial\psi/\partial x_1'|$) that weight the diffraction stack. These quantities and their product are presented in Figures 7.6 and 7.7 for modes q=2,4, respectively. The depth of the scatterer point under consideration is 40 km and the slowness of the incident wave is 0.05 s km^{-1}. For reference, the location of the travel time minimum is shown in Figures 7.6 and 7.7 as a dotted line. Figures 7.6b,d show the travel time sensitivity $\left|\nabla \mathcal{T}^{(2)}\right|^2$ and radiation pattern $W_2^2(\theta)$ factors. Both factors contribute to significant downweighting near the travel time apex, whereas the Jacobian of the transformation of variables, $|\partial\psi/\partial x_1'|$ (Figure 7.6c) is sharply peaked and maximally weights the diffraction stack close to the minimum traveltime. The cumulative product which represents the total weight along the diffraction stack is bimodal with the travel time apex falling away from the global minimum such that at the apex, the diffraction stack receives only ~25% of the maximum weight. In the case of *P-S* back-scattering (q=4) (Figure 7.7), travel time sensitivity and radiation pattern are more favorably positioned in Figures 7.7b,d

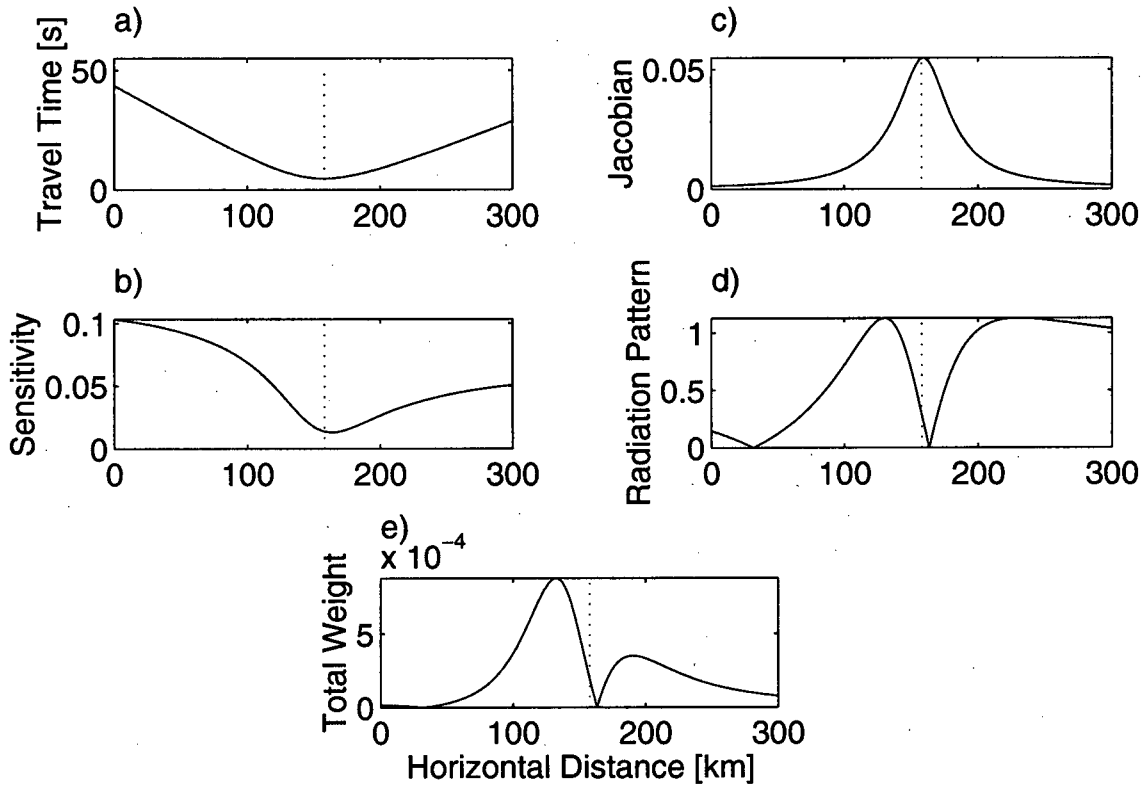

Figure 7.6: Diffraction stack weights for forward-scattered *P-S* interaction (q=2). a) Total travel time $\mathcal{T}^{(2)}$; b) travel time sensitivity $\left|\nabla\mathcal{T}^{(2)}\right|^2$; c) Jacobian of the transformation of variables $|\partial\psi/\partial x_1'|$; d) radiation pattern W_2^2; and e) the product of b), c) and d).

such that the maximum of the total weighting function is in close proximity to the apex of $\mathcal{T}^{(4)}$. The Jacobian (Figure 7.7c) is slightly broadened relative to that in Figure 7.6c. Consequently, the cumulative weighting function, Figure 7.7e, is again bimodal, but the $\mathcal{T}^{(4)}$ apex is now positioned close to the location of maximum weight.

While these weights are appropriate and effective for single point scatterers, they have a rather different efficiency for quasi-planar structures. Since the diffraction hyperbolae are tangent to the travel time locii for planar discontinuities at the hyperbola apex, reconstruction using forward scattered energy extracts a lower proportion of signal from the true arrival. It is therefore more

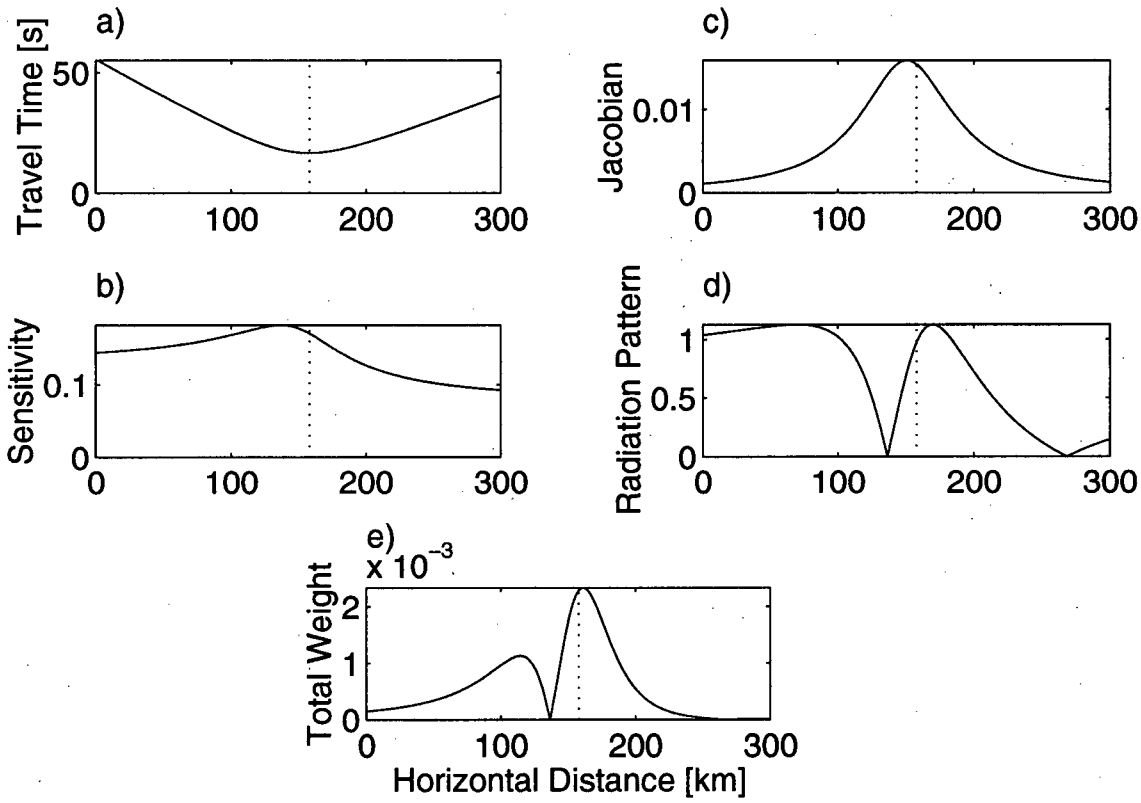

Figure 7.7: Diffraction stack weights for back-scattered *P-S* interaction (q=4). a) Total travel time $\mathcal{T}^{(4)}$; b) travel time sensitivity $\left|\nabla\mathcal{T}^{(4)}\right|^2$; c) Jacobian of the transformation of variables $|\partial\psi/\partial x_1'|$; d) radiation pattern W_2^4; and e) the product of b), c) and d).

prone to contamination from noise and may be more susceptible to incomplete coverage in ψ.

7.8 Experiment IV - Multiple Mode, Multiple Event Inversion

In this experiment, the improvements in model reconstruction incurred through simultaneous inversion of both forward- and back-scattered modes (q=2,3,4,6) are examined. As mentioned above, the inability to fully separate individual scattering modes results in images that suffer from cross-mode contamination (cf. Experiment III). Therefore, it is justified to weight individual mode contributions in the simultaneous inversion on some *a priori* basis which accounts for this

contamination. In particular, relative signal amplitudes as governed by free surface reflection coefficients and the anticipated response of underlying heterogenity must be considered. In the present experiment, these factors have been considered in a somewhat subjective fashion and have been chosen so as to i) downweight the *P-S* (q=4) interaction by 30% to bring the contaminating *S-S* (q=6) interaction structure to approximately comparable levels with the *P-S* (q=4) phantom structure observed in the *S-S* (q=6) interaction image, and ii) upweight the forward-scattered *P-S* (q=2) interaction by a factor of 6 to allow for a more balanced representation of forward-scattering in the simultaneous inversion results.

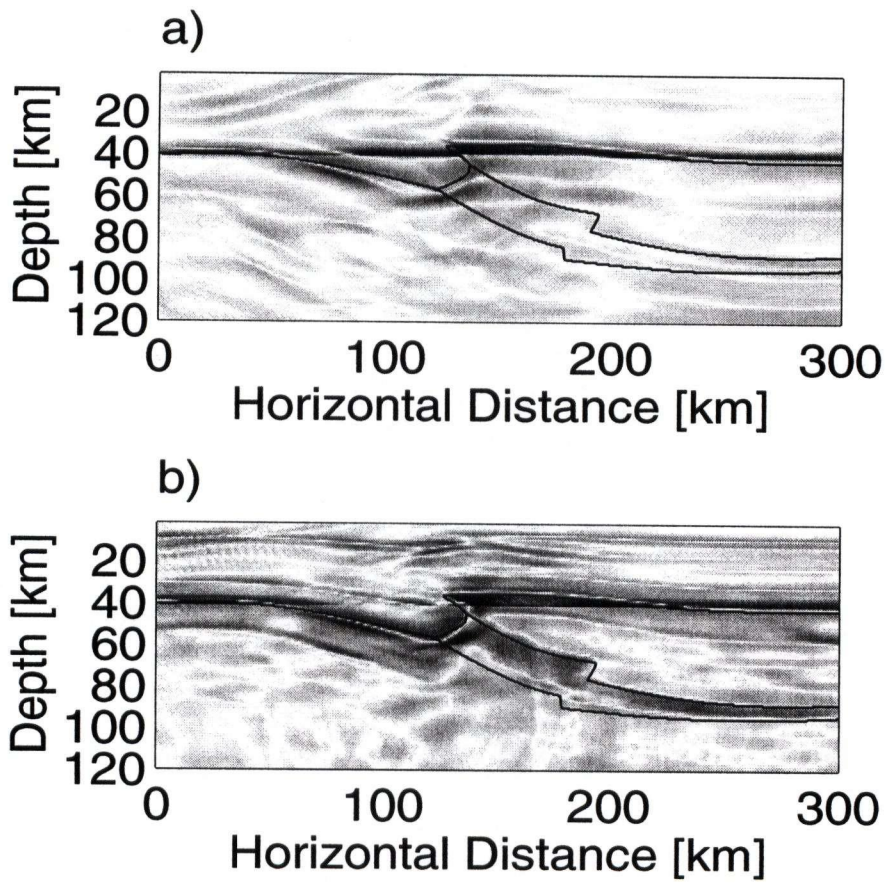

Figure 7.8: Reconstructed velocity pertubations from simultaneous inversion of individually weighted modes from all six events. a) $\Delta\alpha/\alpha$; b) $\Delta\beta/\beta$.

Figures 7.8a,b present the reconstructed *P*- and *S*-velocity perturbations from the inversion of the four individually weighted modes, respectively. In both figures, the Moho and the relict crust are well delineated in reference to model structure. In accordance with the true velocity model (see Table 6.1), the *S*-velocity image identifies the relict crust as a relatively larger perturbation than its *P*-velocity counterpart. Furthermore, in contrast with the images recovered from individual back-scattered waves (i.e., Experiment III), the resulting *S*-velocity perturbation image is now less contaminated by phantom structure leaving the suture zone more clearly evident. In general, the simultaneous inversion of individually weighted scattering interactions realizes a well-constrained, and improved reconstruction of the model.

7.9 Experiment V - Noise and Spatial Aliassing Issues

The previous experiments have employed noise free data sets to investigate the inversion/migration methodology developed in *Paper I*. The ability of the approach to perform in a situation where data quality and recording geometry are more representative of typical field experiments is now examined. The idealized suture model has been altered to include a surface layer of 6 km average thickness (Figure 7.9a). The layer is parameterized by *P*-wave and *S*-wave velocity and density values of 5.2 km s^{-1}, 2.8 km s^{-1}, and 2.5 g cm^{-3}, respectively, and exhibits random undulations of maximum amplitude 1.2 km which have give rise to strong near-surface body-wave and surface-wave scattering (see Figures 7.9b,c). In addition, a random selection of 60 stations has been taken from the previous 120 stations resulting in receiver spacings between 3 km and 15 km, and data sections have been contaminated with Gaussian noise of zero mean and a standard deviation equivalent to 5% of the amplitude of the incident wave. Given the frequency content of the incident wavefield, it is expected that the resulting images will suffer to some degree from the effects of spatial aliassing.

Figures 7.9d,e present the *P*- and *S*-velocity images using the same weighted mode contribution and event selection as Experiment IV. In both images, the Moho and normal-relict crustal discontinuities remain well delineated. The *S*-velocity image also accurately retrieves the remaining discontinuities of the suture zone. Scattering from the near-surface layer has introduced to the images an additional source of noise that has been mapped back to the near surface. Additive white noise has had a relatively minor effect on the reconstruction since it is largely cancelled through the integration in equation (7.1). Figure 7.9d,e do suffer from spatial aliasing manifest

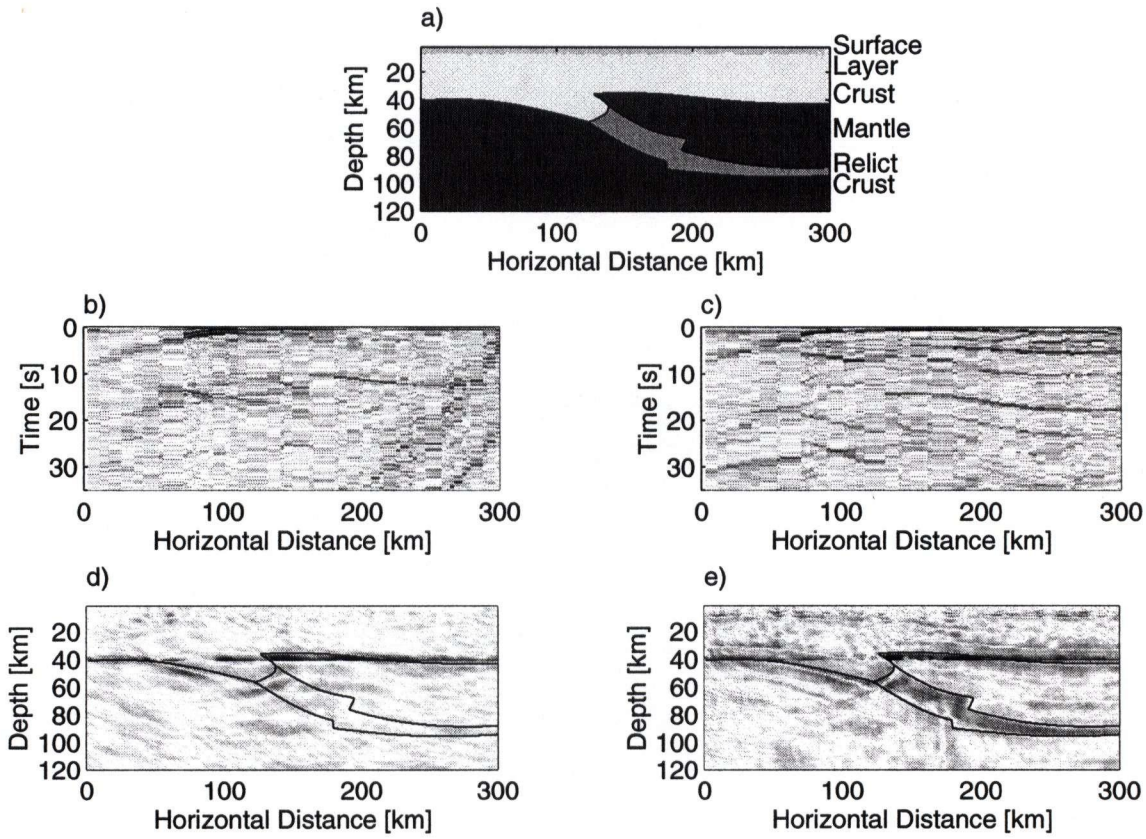

Figure 7.9: Reconstructed velocity pertubations from simultaneous inversion of individually weighted modes from all events including a model with an additional surface layer, and data with additive noise and reduced irregular station distribution. a) Revised subduction-suture model; b) Preprocessed (but prior to filtering by $F(\omega)$) Δu_3 synthetic data section (p_1^0=-0.07 s km^{-1}) generated for model shown in a); c) As in b) but for Δu_1; d) $\Delta\alpha/\alpha$; e) $\Delta\beta/\beta$.

through the high wavenumber "speckle" which is, however, most prominent at shallow levels and diminishes with depth so as not to pose significant impediment in the reconstruction of lower crustal and mantle structures.

Chapter 8

Concluding Remarks

Part I of this thesis presents the results from a number of analyses involving teleseismic data collected in southern Alberta. Results from travel-time tomography document a high velocity anomaly underlying a substantial portion of the southern Hearne Province which is interpreted to represent deep-seated lithospheric structure. These results suggest that the bulk of the lithosphere has remained intact, and that the anomously high mantle conductivity values noted in magnetotelluric surveys are probably the result of connected hydrous minerals or some other conductive species introduced during subduction processes responsible for a thickened lithospheric root. Shear wave splitting results reveal a relatively uniform set of splitting parameters with an average polarization direction that broadly corresponds to both the (presumably) preserved fossil strain fields arising from the ca. 1.8 Ga, NW-SE shortening of the Hearne Province, and to the absolute motion of the North American Plate. Processing of radial receiver functions yield Moho depth estimates that are fairly uniform in the northern sections of the array, but reveal crustal thickening to the south within Medicine Hat Block.

Part II of this thesis presents results from a number of simulations that test the inverse scattering/migration methodology for teleseismic waves developed in *Paper I*. The flexibility of the method has been exploited to investigate the roles that different scattering mode and event combinations play in the recovery of structure corresponding to an idealized lithospheric suture. In

particular, it demonstrates: i) the contrasting and complementary sensitivity of forward- and back-scattered modes to structure; ii) the reduction in problem null-space that accompanies improved source coverage; iii) improvements in structural recovery incurred through simultaneous treatment of different scattering modes, and iv) the robustness of the approach in the presence of typical signal-to-noise levels and irregular station geometry.

References

Beaumont, C., and G. Quinlan, A geodynamic framework for interpreting crustal-scale seismic-reflectivity patterns in compressional orogens, *Geophys. J. Int.*, 116, 754-783, 1994.

Beylkin, G., Imaging of discontinuities in the inverse scattering problem by inversion of a causal generalized Radon transform, *J. Math. Phys., 26*, 99-108, 1985.

Bickford, M.E., K.D. Collerson, and J.F. Lewry, Crustal history of the Rae and Hearne provinces, southwestern Canadian Shield, Saskatchewan: Constraints from geochronologic and isotopic data, *Precambrian Research*, 68, 1-21, 1994.

Boerner, D.E., R.D. Kurtz, J.A. Craven, G.M. Ross, F.W. Jones, and W.J. Davis, Electrical conductivity in the Precambrian lithosphere of Western Canada, *Science*, 283, 668-670, 1999.

Boerner, D.E., R.D. Kurtz, J.A. Craven, G.M. Ross, and F.W. Jones, A synthesis of electromagnetic studies in the Lithoprobe Alberta Basement Transect, southwestern Alberta, *Can. J. Earth Sci.*, 37, 1509-1534, 2000.

Bostock, M.G., Mantle stratigraphy and evolution of the Slave province, *Geophys. J. Int.*, 134, 21183-21200, 1998.

Bostock, M.G., and J.F. Cassidy, Variations in *SKS* splitting across western Canada, *Geophys. Res. Lett.*, 22, 5-8, 1995.

Bostock, M.G., and S. Rondenay, Migration of scattered teleseismic body waves, *Geophys. J. Int.*, 137, 732-746, 1999.

Bostock, M.G., S. Rondenay, and J. Shragge, Multi-parameter 2-D inversion of scattered teleseismic body-waves - I. Theory for oblique incidence, submitted to *J. Geophys. Res.*, 2000.

Bostock, M.G., and J.C. VanDecar, Upper mantle structure of the northern Cascadia subduction zone, *Can. J. Earth Sci.*, 32, 1-12, 1995.

Burchfiel, B.C., D.S. Cowan, and G.A. Davis, Tectonic overview of the Cordilleran orogen in the western United States, In: Burchfiel, B.C., P.W. Lipman, and M.L. Zoback, eds., The Geology of North America, The Cordilleran Orogen: Conterminous United States, Geological Society of America, 447-512, 1992.

Calvert, A.J., E.W. Sawyer, W.J. Davis, and J.N. Ludden, Archaen subduction inferred from seismic images of a mantle suture in the Superior Province, *Nature*, 375, 670-673, 1995.

Chandra, N.N., and G.L. Cumming, Seismic refraction studies in western Canada, *Can. J. Earth Sci.*, 9, 1099-1109, 1972.

Clowes, R.M., and E.R. Kanasewich, Digital filtering of deep crustal seismic reflections, *Can. J. Earth Sci.*, 9, 434-451, 1972.

Clowes, R.M., M.J.A. Burianyk, A.R. Gorman, and E.R. Kanasewich, Crustal velocity structure from SAREX the Southern Alberta Refraction Experiment, submitted to *Can. J. Earth Sci.*, 2001.

Cook, F.A., A.J. van der Velden, K.W. Hall, and B.J. Roberts, Tectonic delamination and subcrustal imbrication of the Precambrian lithosphere in northwestern Canada mapped by Lithoprobe, *Geology*, 26, 839-842, 1998.

Deiss, C., Cambrian geography and sedimentation in the central Cordilleran subduction zone, *Geol. Soc. Amer. Bull.*, 52, 1084-1116, 1941.

Eaton, D.W., G.M. Ross, and R.M. Clowes, Seismic reflection and potential-field studies of the Vulcan structure, western Canada: A Paleoproterozoic Pyrenees?, *J. Geophys. Res.*, 104, 255-269, 1999.

Eaton, D.W., G.M. Ross, F.A. Cook, and A. VanderVelden, Seismic imaging of the upper mantle beneath the Rocky Mountain foreland, southwestern Alberta, *Can. J. Earth Sci.*, 37, 1493-1507, 2000.

Forgues, E., and G. Lambaré, Parameterization study for acoustic and elastic ray+Born inversion, *Journal of Seismic Exploration*, 6, 253-277, 1997.

Frederiksen, A.W., M.G. Bostock, and J.F. Cassidy, *S*-wave velocity structure of the Canadian upper mantle, *Phys. Earth Planet. Int.*, in press, 2001.

Fouch, M.J., K.M. Fischer, E.M. Parmentier, M.E. Wysession, and T.J. Clarke, Shear wave splitting, continental keels, and patterns of mantle flow, *J. Geophys. Res.*, 105, 6255-6276, 2000.

Fullsack, P., An arbitrary Langrangian-Eulerian formulation for creeping flows and its application in tectonic models, *Geophys. J. Int.*, 120, 1-23, 1995.

Gorman, A.R., R.M. Clowes, R.M. Ellis, T.J. Henstock, G.D. Spence, G.R. Keller, A.R. Levander, C.M. Snelson, M.J.A. Burianyk, E.R. Kanasewich, I. Asudeh, Z. Hajnal, and K.C. Miller, Deep Probe - Imaging the roots of western North America, submitted to *Can. J. Earth Sci.*, 2001.

Gorman, A.R., Deep Probe: Investigating the lithosphere of western North America with refraction seismology, Ph.D. thesis, 230 pp., Univ. of British Columbia, Vancouver, October 2000.

Gurrola, H., G.E. Baker, and J.B. Minster, Simultaneous time-domain deconvolution with application to the computation of receiver functions, *Geophys. J. Int.*, 120, 537-543, 1995.

Hestenes, M.R., and E. Stiefel, Methods of conjugate gradients for solving linear systems, *Nat. Bur. Standards J. Res.*, 49, 409-436, 1952.

Hoffman, P.F., United plates of America, the birth of a craton: Early Proterozoic assembly and growth of Laurentia, *Ann. Rev. Earth Planet. Sci.*, 16, 543-603, 1988.

Hoffman, P.F., Subdivision of the Churchill province and extent of the Trans-Hudson orogen, In: The Early Proterozoic Trans-Hudson orogen of North America, Lewry, J.F., and M.R. Stauffer, eds., Geol. Assoc. Canada, Spec. Pub. 37, 15-39, 1990.

Hyndman, R.D., Dipping seismic reflections, electrically conductive zones, and trapped water in the crust over a subducting plate, *J. Geophys. Res.*, 93, 13391-13405, 1988.

Jordan, T.H., Structure and formation of the continental tectosphere, *J. Petrology*, Special Lithosphere Issue, 11-37, 1988.

Kanasewich, E.R., R.M. Clowes, and C.H. McLoughlan, A buried Precambrian rift in western Canada, *Tectonophysics*, 8, 513-527, 1969.

Kanasewich, E.R., and G.L. Cumming, Near-vertical-incidence seismic reflections from the 'Conrad' discontinuity, *J. Geophys. Res.*, 70, 3441-3446, 1965.

Karato, S., The role of hydrogen in the electrical conductivity of the upper mantle, *Nature*, 347, 272-273, 1990.

Kennett, B.L.N., The removal of free surface interactions from three-component seismograms, *Geophys. J. Int.*, 104, 153-163, 1991.

Kennett, B.L.N., and E.R. Engdahl, Travel times for global earthquake location and phase identification, *Geophys. J. Int.*, 105, 429-465, 1991.

Kosloff, D., D. Kessler, A.Q. Filho, E. Tessmer, A. Gehlle, and R. Strahilevits, Solutions of the equations of dynamic elasticity by a Chebychev spectral method, *Geophysics*, 55, 734-748, 1990.

Langston, C.A., Structure under Mount Rainier, Washington, inferred from teleseismic body waves, *J. Geophys. Res.*, 84, 4749-4762, 1979.

Lemieux, S., G.M. Ross, and F.A. Cook, Crustal geometry and tectonic evolution of the Archean crystalline basement beneath the southern Alberta Plains, from new seismic reflection and potential-field studies, *Can. J. Earth Sci.*, 37, 1473-1491, 2000.

Lewry, J.F., Z. Hajnal, A. Green, S.B. Lucas, D. White, M.R. Stauffer, K.E. Ashton, W. Weber, and R.M. Clowes, Structure of a Paleoproterozoic continent-continent collision zone; a Lithoprobe seismic reflection profile across the Trans-Hudson Orogen, Canada, *Tectonophysics*, 232, 143-160, 1994.

Lucas, S.V., A. Green, Z. Hajnal, D. White, J. Lewry, K. Ashton, W. Weber, and R.M. Clowes, Deep seismic profile across a Proterozoic collision zone: Suprises at depth, *Nature*, 363, 339-342, 1993.

Marquering, H., F.A. Dahlen, and G. Nolet, Three-dimensional sensitivity kernels for finite-frequency traveltimes: The banana-doughnut paradox, *Geophys. J. Int.*, 137, 805-815, 1999.

Miller, D., M. Oristaglio, and G. Beylkin, A new slant on seismic imaging: Migration and integral geometry, *Geophysics, 52*, 943-964, 1987.

Minster, J.B., and T.H. Jordan, Present-day plate motions, *J. Geophys. Res.*, 83, 5331-5354, 1978.

O'Neill, J.M., and D.A. Lopez, Character and regional significance of Great Falls Tectonic Zone, east-central Idaho and west-central Montana, *Am. Ass. Petr. Geol. Bull.*, 69, 437-447, 1985.

Pfiffner, O.A., W. Frei, P. Valasek, M. Stäuble, L. Levato, L. DuBois, S.M. Schmid, and S.B. Smithson, Crustal shortening in the Alpine Orogen: Results from deep seismic reflection profiling in the eastern Swiss Alps, line NFP 20-east, *Tectonics*, 9, 1327-1355, 1990.

Pysklywec, R.N., and J.X. Mitrovica, Mantle flow mechanisms of epeirogeny and their possible role in the evolution of the Western Canadian Sedimentary Basin, *Can. J. Earth Sci.*, 37, 1535-1548, 2000.

Revenaugh, J., A scattered-wave image of subduction beneath the transverse ranges, *Science*, 268, 1888-1892, 1995.

Roberts, J.J., A.G. Duba, E.A. Mathez, T.J. Shankland, and R. Kinzler, Carbon-enhanced electrical conductivity during fracture of rocks, *J. Geophys. Res.*, 104, 737-747, 1999.

Rondenay, S., Teleseismic imaging of the southeastern Canadian Shield and the Cascadia subduction zone, Ph.D. thesis, 118 pp., Univ. of British Columbia, Vancouver, December 2000.

Rondenay, S., M.G. Bostock, and J. Shragge, Multi-parameter 2-D inversion of scattered teleseismic body-waves - III. Application to CASC93, submitted to *J. Geophys. Res.*, 2000.

Ross, G.M., Assembly of the southwestern Laurentian Craton, In: Lithoprobe; Alberta Basement Transects; Ross, G.M. ed., Lithoprobe Secretariat, University of British Columbia, *Lithoprobe Report* 59, 23-34, 1997.

Ross, G.M., D.W. Eaton, D.E. Boerner, and W. Miles, Tectonic entrapment and its role in the evolution of continental lithosphere: An example from the Precambrian of western Canada, *Tectonics*, 19, 116-134, 2000.

Ross, G.M., B. Milkereit, D. Eaton, D. White, E.R. Kanasewich, and M.J.A. Burianyk, Paleoproterozoic collisional orogen beneath the Western Canada Sedimentary Basin imaged by Lithoprobe crustal seismic-reflection data, *Geology*, 23, 195-199, 1995.

Ross, G.M., R.R. Parrish, M.E. Villeneuve, and S.A. Bowring, Geophysics and geochronology of the crystalline basement of the Alberta Basin, western Canada, *Can. J. Earth. Sci.*, 28, 512-522, 1991.

Ryberg, T. and M. Weber, Receiver function arrays: A reflection seismic approach, *Geophys. J. Int.*, 141, 1-11, 2000.

Shragge, J., M.G. Bostock, and S. Rondenay, Multi-Parameter 2-D inversion of scattered teleseismic body-waves - II. Synthetic examples, submitted to *J. Geophys. Res.*, 2000.

Silver, P.G., and W.W. Chan, Shear wave splitting and subcontinental mantle deformation, *J. Geophys. Res.*, 96, 16429-16454, 1991.

Van der Lee, S., and G. Nolet, The upper-mantle *S*-velocity structure of North America, *J. Geophys. Res.*, 102, 22815-22838, 1997.

VanDecar, J.C., Upper-mantle structure of the Cascadia subduction zone from non-linear teleseismic traveltime inversion, Ph.D. thesis, 165 pp., Univ. of Washington, Seattle, June 1991.

VanDecar, J.C., and R.S. Crosson, Determination of the teleseismic relative phase arrival times using multi-channel cross-correlation and least squares, *Bull. Seismol. Soc. Am.*, 80, 150-169, 1990.

Vinnik, L.P., L.I. Makeyeva, A. Milev, and A. Yusenko, Global patterns of azimuthal anisotropy and deformations in the continental mantle, *Geophys. J. Int.*, 111, 433-447, 1992.

Wolfe, C.J., and P.G. Silver, Seismic anisotropy of oceanic upper mantle; shear wave splitting methodologies and observations, *J. Geophys. Res.*, 103, 749-771, 1998.

Zandt, G., and T.J. Owens, Comparison of crustal profiles determined by seismic refraction and teleseismic methods, *Tectonophysics*, 128, 155-161, 1986.

Zhu, L., and H. Kanamori, Moho depth variation in southern California from teleseismic receiver functions, *J. Geophys. Res.*, 105, 2969-2980, 2000.

Appendix A

Data set employed in Chapter 3 analyses

Table A.1: Events used in the analyses of Chapter 3. Individual techniques are denoted by: TTI-*P*, *P*-wave travel-time inversion; RF, receiver functions; SWS, shear wave splitting.

Date YY:MM:DD	Time hh:mm:ss.s	Latitude °N	Longitude °E	Depth km	m_b	TTI-*P*	RF	SWS
96:05:02	13:34:28	-4.548	154.833	500	5.6		X	X
96:06:17	11:22:18	-7.137	122.589	587	6.6		X	
96:07:20	07:41:15	-19.820	-177.643	357	5.7		X	
96:08:05	22:38:22	-20.690	-178.310	550	6.4		X	
96:10:19	14:53:48	-20.410	-178.510	425	5.8		X	X
96:11:05	09:41:34	-31.160	179.998	369	6.4		X	X
97:09:04	04:23:37	-26.569	178.336	625	6.3		X	X
98:03:29	19:48:16	-17.552	-179.092	537	6.5		X	X
98:05:16	02:22:03	-22.227	-179.519	586	6.1		X	X
98:07:29	07:14:24	-32.312	-71.286	51	6.3		X	
98:08:02	04:40:46	39.573	76.999	69	5.6		X	
98:08:04	18:59:20	-0.593	-80.393	33	6.2		X	
98:08:05	10:42:21	56.164	163.360	33	5.2	X		
98:08:09	05:27:43	53.008	171.139	25	5.3	X		
98:08:11	02:07:49	25.014	123.017	141	5.0	X		
98:08:13	06:16:51	53.068	171.106	33	5.0	X		
98:08:18	18:00:12	45.852	149.116	116	5.4	X		
98:08:20	06:40:55	28.932	139.329	441	6.1	X	X	
98:08:20	09:36:34	45.561	136.926	351	5.2	X		
98:08:20	14:56:40	51.531	175.389	33	5.4	X		
98:08:20	15:00:08	51.618	175.248	33	5.6	X	X	
98:08:23	05:36:12	14.697	120.046	70	6.1	X		
98:08:23	13:57:15	11.663	-88.038	55	5.7	X	X	
98:08:25	07:41:40	30.079	88.109	33	5.3	X		
98:08:27	16:51:45	19.274	-108.446	10	5.0	X		
98:08:28	15:31:38	51.437	175.526	33	5.5	X		
98:08:28	23:46:43	35.522	139.879	76	5.2	X		

Table A.1: (Continued)

Date YY:MM:DD	Time hh:mm:ss.s	Latitude °N	Longitude °E	Depth km	m_b	TTI-*P*	RF	SWS
98:08:30	01:48:08	17.092	148.133	33	6.0	X	X	
98:08:30	14:34:43	53.669	161.867	33	5.5	X		
98:09:01	01:19:37	-17.555	-174.771	220	5.3	X		
98:09:01	08:29:12	-28.049	-70.439	87	4.6	X		
98:09:01	14:33:41	-16.758	-173.597	33	5.4	X		
98:09:02	08:37:29	5.410	126.764	50	6.6	X	X	X
98:09:03	06:43:03	39.539	77.260	33	5.1	X		
98:09:03	07:58:21	39.716	140.760	38	5.7	X	X	
98:09:03	17:37:58	-29.450	-71.715	27	6.2	X	X	
98:09:03	18:15:56	27.850	86.941	33	5.6	X		
98:09:05	05:16:17	-6.646	155.209	37	5.5	X		
98:09:07	00:23:02	-32.347	-111.950	10	5.3	X		
98:09:07	00:39:30	-36.240	-97.711	10	5.2	X		
98:09:07	02:35:03	-5.766	152.061	41	5.2	X		
98:09:08	09:10:03	13.257	144.007	141	5.8	X	X	X
98:09:09	11:27:59	40.035	15.980	10	5.2	X		
98:09:10	09:51:24	-20.028	-70.378	33	4.9	X		
98:09:12	09:03:48	-24.512	-67.119	187	5.1	X		
98:09:12	10:58:04	-14.233	-72.615	91	5.3	X		
98:09:14	23:16:46	51.618	-173.150	33	5.7	X	X	
98:09:15	07:24:06	38.346	140.508	50	5.1	X		
98:09:15	08:35:51	-5.624	151.637	83	5.6	X	X	
98:09:16	02:12:02	-6.580	154.868	87	5.4	X		
98:09:16	11:09:14	-24.047	-66.744	175	4.9	X		
98:09:16	11:28:56	-3.242	-79.348	104	4.9	X		
98:09:17	16:41:20	-38.294	-93.623	10	5.3	X		
98:09:17	18:14:25	30.593	137.557	487	4.5	X		
98:09:18	03:51:13	43.212	148.097	10	5.1	X		
98:09:20	00:36:46	-21.392	-174.709	100	5.1	X		
98:09:21	13:00:04	48.360	148.771	396	4.3	X		
98:09:22	01:16:55	11.822	143.154	9	5.8	X	X	
98:09:24	18:53:40	46.313	106.288	33	5.5	X		
98:09:27	11:07:16	-20.270	-175.876	207	5.2	X		
98:09:28	13:34:30	-8.194	112.413	152	6.4			X
98:09:28	19:23:23	3.840	126.407	30	5.8	X		
98:09:29	22:14:49	44.209	20.080	10	5.2	X		
98:10:01	03:41:13	13.738	-45.565	10	5.4	X		

Table A.1: (Continued)

Date YY:MM:DD	Time hh:mm:ss.s	Latitude °N	Longitude °E	Depth km	m_b	TTI-*P*	RF	SWS
98:10:01	20:44:06	9.675	-82.443	31	5.3	X		
98:10:02	12:49:35	27.268	101.016	48	5.2	X		
98:10:03	11:15:42	28.505	127.615	227	5.6	X	X	
98:10:06	12:27:41	37.247	21.107	10	5.0	X		
98:10:07	06:53:14	21.536	143.057	300	5.2	X		
98:10:07	13:41:01	12.902	146.719	34	5.0	X		
98:10:08	04:51:42	-16.119	-71.404	136	6.1	X	X	
98:10:09	05:37:52	-15.393	-173.392	33	5.0	X		
98:10:09	11:54:36	11.321	-86.451	69	5.5	X		
98:10:10	04:12:08	-33.518	-72.078	33	5.3	X		
98:10:10	20:18:39	23.728	142.936	33	4.9	X		
98:10:11	12:04:54	-21.040	-179.110	624	5.4	X		
98:10:11	21:44:16	-27.329	-63.335	583	5.3	X		
98:10:12	07:36:39	-15.278	-173.579	77	4.9	X		
98:10:13	18:13:04	-20.861	-178.770	600	4.5	X		
98:10:13	20:41:13	40.027	143.297	33	5.4	X		
98:10:14	01:36:19	60.711	-44.050	10	5.1	X		
98:10:14	02:54:04	-5.915	151.036	33	5.5	X	X	
98:10:18	01:39:01	24.718	141.237	110	5.5	X	X	
98:10:18	08:33:54	19.285	145.341	152	5.4	X		
98:10:18	22:09:19	86.283	75.609	10	5.2	X		
98:10:19	23:57:33	-21.254	-68.969	124	4.7	X		
98:10:20	11:52:40	-20.594	-174.299	33	5.1	X		
98:10:23	01:48:51	-2.423	-76.359	147	5.3	X		
98:10:24	08:27:12	-17.719	-175.222	261	5.1	X		
98:10:25	03:54:39	-17.974	-69.592	33	5.0	X		
98:10:25	20:06:05	36.438	68.585	61	5.1	X		
98:10:26	02:34:57	-21.224	-178.905	574	4.9	X		
98:10:27	11:33:37	33.489	141.398	33	5.3	X		
98:10:28	21:39:52	11.985	143.528	33	5.5	X		
98:10:31	12:45:50	-17.881	-178.318	577	4.8	X		
98:10:31	13:38:50	29.328	142.042	19	5.1	X		
98:10:31	14:03:32	53.049	157.859	53	5.2	X		
98:11:02	23:10:59	43.665	147.620	58	5.5	X	X	
98:11:04	02:54:13	52.094	-176.143	35	5.1	X		
98:11:05	03:45:17	-10.322	-78.364	51	5.4	X		
98:11:05	20:09:55	-15.613	-177.990	33	5.0	X		

Table A.1: (Continued)

Date YY:MM:DD	Time hh:mm:ss.s	Latitude °N	Longitude °E	Depth km	m_b	TTI-*P*	RF	SWS
98:11:06	12:24:07	-21.806	-67.162	210	4.9	X		
98:11:07	05:35:41	41.592	142.109	79	4.7	X		
98:11:09	04:57:41	-21.148	-174.452	53	5.2	X		
98:11:10	00:12:03	27.176	142.730	33	5.0	X		
98:11:10	17:45:12	-22.027	-68.239	118	4.7	X		
98:11:11	23:35:46	53.511	-164.530	33	4.9	X		
98:11:11	23:36:33	1.079	-85.275	33	5.5	X		
98:11:13	17:38:58	-21.572	-68.222	123	5.4	X		
98:11:14	14:23:15	11.709	143.248	33	5.3	X		
98:11:15	02:44:12	-21.589	-176.504	149	5.9	X	X	X
98:11:15	04:51:42	-4.075	-104.181	10	4.8	X		
98:11:15	07:58:14	13.001	143.607	142	4.9	X		
98:11:15	08:23:08	-9.344	-71.292	596	4.7	X		
98:11:15	23:08:33	37.658	137.320	21	4.9	X		
98:11:17	03:16:08	-26.830	-113.290	10	5.4	X		
98:11:17	03:57:58	7.666	-82.780	17	5.2	X		
98:11:17	17:08:02	-21.695	-179.131	600	5.1	X		
98:11:17	22:27:32	22.675	120.959	33	5.2	X		
98:11:18	07:32:53	-10.551	165.116	62	4.8	X		
98:11:19	07:28:07	-9.045	-78.618	73	4.7	X		
98:11:19	15:39:19	22.605	125.783	10	5.8	X	X	
98:11:20	18:14:32	-28.384	-112.814	10	4.8	X		
98:11:20	21:23:38	-16.291	-178.088	438	5.2	X		
98:11:21	16:59:47	49.233	89.186	10	5.2	X		
98:11:22	12:25:37	52.200	178.888	144	4.8	X		
98:11:22	19:01:10	27.242	125.715	253	4.4	X		
98:11:23	09:30:19	-23.716	-70.512	33	5.5	X	X	
98:11:23	12:15:50	-18.184	-174.974	209	5.2	X		
98:11:23	19:48:10	37.979	141.479	79	5.4	X		
98:11:23	19:58:25	45.080	147.162	140	4.8	X		
98:11:24	01:06:11	-22.625	-69.243	80	5.3	X		
98:11:24	21:24:31	-16.000	-172.703	33	5.2	X		
98:11:24	23:54:46	-16.515	-174.751	223	5.4	X		
98:11:25	18:05:25	-7.859	158.622	48	5.9	X	X	
98:11:27	10:27:02	-32.140	-69.328	127	5.2	X		
98:11:28	09:58:09	-7.589	-74.416	149	5.3	X		
98:11:28	15:21:05	-15.363	172.964	33	5.4	X		

Table A.1: (Continued)

Date YY:MM:DD	Time hh:mm:ss.s	Latitude °N	Longitude °E	Depth km	m_b	TTI-*P*	RF	SWS
98:11:29	17:14:00	48.132	148.441	396	4.9	X		
98:11:30	20:18:28	14.096	145.451	115	4.6	X		
98:12:01	10:38:45	53.099	-164.338	22	5.6	X	X	
98:12:02	07:11:03	-33.457	-109.346	10	5.4	X		
98:12:04	18:50:07	43.620	-28.760	10	4.8	X		
98:12:05	01:12:47	52.121	-169.412	33	5.4	X		
98:12:05	08:06:51	10.985	-86.163	96	4.9	X		
98:12:06	23:31:00	-21.059	-179.133	600	4.9	X		
98:12:08	02:32:57	18.819	-64.046	30	5.6	X		
98:12:09	07:35:49	19.243	145.437	151	4.9	X		
98:12:10	08:21:14	-7.952	-71.416	649	5.1	X		
98:12:11	08:37:50	-31.266	-68.918	118	5.5	X	X	
98:12:11	21:42:46	-16.597	-172.758	33	5.2	X		
98:12:13	17:31:58	13.345	-44.845	10	5.3	X		
98:12:13	20:07:52	13.338	-44.949	10	4.9	X		
98:12:14	04:30:56	30.923	137.654	464	4.9	X		
98:12:14	16:25:24	-38.214	-71.033	138	5.4	X		
98:12:16	00:18:45	31.287	131.286	42	5.5	X	X	
98:12:23	15:14:07	17.509	-94.660	145	4.5	X		
98:12:26	11:29:09	10.604	-63.544	33	5.4	X		
98:12:27	00:38:26	-21.632	-176.376	144	6.1	X	X	X
98:12:28	07:23:31	20.780	-74.673	10	5.6	X		
98:12:30	03:32:37	-1.646	-77.881	169	5.0	X		
99:01:01	16:20:30	36.139	141.636	33	5.1	X		
99:01:07	11:38:07	43.827	148.233	56	5.0	X		
99:01:07	18:13:41	67.768	141.306	33	5.4	X		
99:01:07	22:16:07	-20.480	-173.988	33	4.9	X		
99:01:09	03:05:37	44.390	147.313	119	5.8	X		
99:01:11	10:48:50	52.166	159.626	33	5.3	X		
99:01:12	02:32:25	26.741	140.170	441	5.9		X	
99:01:12	08:49:20	-5.421	151.681	43	5.5		X	
99:01:16	03:01:01	50.749	-169.920	33	5.4	X		
99:01:16	09:06:36	12.308	144.105	33	5.2	X		
99:01:17	05:29:12	43.185	147.525	52	5.2	X		
99:01:17	15:28:35	13.232	145.528	33	5.2	X		
99:01:19	03:35:33	-4.596	153.235	114	5.8	X		
99:01:20	07:38:35	52.291	179.801	170	4.7	X		

Table A.1: (Continued)

Date YY:MM:DD	Time hh:mm:ss.s	Latitude °N	Longitude °E	Depth km	m_b	TTI-*P*	RF	SWS
99:01:20	13:43:48	-17.752	-178.930	600	4.6	X		
99:01:20	23:10:04	-14.801	-75.865	33	5.2	X		
99:01:21	22:02:16	38.649	142.904	33	5.3	X		
99:01:24	00:37:04	30.618	131.086	33	6.1	X	X	
99:01:24	07:01:58	-21.132	-174.659	33	5.7	X	X	
99:01:24	13:15:52	54.476	161.458	33	5.3	X		
99:01:25	10:37:13	-18.026	-178.445	640	5.0	X		
99:01:25	18:19:16	4.461	-75.724	17	5.9	X	X	
99:01:25	22:40:16	4.370	-75.682	10	5.5	X		
99:01:26	12:30:49	-20.515	-174.207	41	5.5	X	X	
99:01:26	16:18:30	-17.762	-178.809	596	4.7	X		
99:01:27	08:20:31	48.376	156.213	71	5.2	X		
99:01:27	10:13:53	6.711	-82.678	10	5.4	X		
99:01:28	08:10:05	52.886	-169.123	67	6.3	X	X	
99:01:30	03:51:05	41.674	88.463	23	5.9	X	X	
99:01:31	05:07:13	43.157	46.841	33	5.3	X		
99:01:31	16:51:51	37.148	141.339	44	5.3	X		
99:01:31	19:29:11	43.455	146.960	33	5.6	X	X	
99:02:04	19:43:14	1.083	-30.545	10	4.9	X		
99:02:05	11:39:45	-12.616	166.966	213	5.7	X	X	
99:02:05	14:37:53	47.505	147.158	407	5.4	X		
99:02:06	13:36:12	53.561	160.402	38	5.2	X		
99:02:06	17:45:24	19.200	121.265	33	5.4	X		
99:02:06	21:47:59	-12.853	166.697	90	6.3	X	X	X
99:02:09	10:38:47	-15.543	-173.343	33	5.0	X		
99:02:10	09:22:35	-21.706	-178.842	549	5.1	X		
99:02:12	17:44:48	44.474	149.678	33	5.6	X		
99:02:14	11:22:37	44.506	149.710	33	5.7	X	X	
99:02:14	21:12:24	-15.507	167.996	10	5.9	X	X	
99:02:15	09:41:52	-18.065	-178.530	624	4.7	X		
99:02:16	14:56:40	15.647	-87.130	10	5.2	X		
99:02:17	21:58:54	-21.143	-70.040	33	5.6	X	X	
99:02:19	19:10:00	85.573	87.037	10	5.1	X		
99:02:21	18:14:37	43.214	46.825	65	5.1	X		
99:02:22	08:02:11	86.278	73.394	10	5.2	X		
99:02:23	12:23:43	53.785	171.134	24	4.9	X		
99:02:23	18:56:56	-20.804	-174.071	36	5.3	X		

Table A.1: (Continued)

Date YY:MM:DD	Time hh:mm:ss.s	Latitude °N	Longitude °E	Depth km	m_b	TTI-*P*	RF	SWS
99:02:24	05:18:54	18.053	146.523	33	5.4	X		
99:02:24	19:11:33	13.609	-90.697	85	4.9	X		
99:02:25	15:35:17	85.671	83.420	10	4.8	X		
99:02:25	18:58:29	51.604	104.865	10	5.9		X	
99:02:26	05:18:18	39.151	139.867	34	5.2	X		
99:03:02	07:12:20	35.592	141.751	33	5.4	X		
99:03:02	17:45:55	-22.717	-68.503	111	5.8	X	X	
99:03:02	21:15:29	51.591	179.538	72	5.3	X		
99:03:04	08:52:01	5.397	121.937	33	6.4		X	
99:03:05	00:33:46	-20.423	-68.901	111	5.7	X	X	
99:03:05	03:35:14	-34.673	-69.600	10	5.2	X		
99:03:06	20:28:53	-21.734	-179.465	603	5.4	X		
99:03:07	01:03:42	42.939	145.906	33	5.2	X		
99:03:07	20:35:44	-15.766	-179.526	33	5.4	X		
99:03:08	05:40:00	52.129	159.482	50	5.4	X		
99:03:08	05:57:52	52.132	159.529	55	5.3	X		
99:03:08	12:25:48	52.056	159.520	57	5.7	X	X	
99:03:10	13:12:55	52.432	-31.849	10	5.2	X		
99:03:12	20:42:35	-19.292	-68.847	118	5.1	X		
99:03:13	01:26:33	85.692	84.797	10	5.3	X		
99:03:18	17:55:43	41.097	142.971	41	5.9	X	X	
99:03:18	21:49:17	-12.040	-75.700	116	5.1	X		
99:03:19	06:38:50	13.224	-87.692	191	4.9	X		
99:03:20	10:47:45	51.587	-177.668	33	6.3	X	X	
99:03:21	15:24:07	85.634	86.819	10	5.4	X		
99:03:21	16:16:02	55.896	110.214	10	5.5	X	X	
99:03:21	16:17:03	55.942	110.272	10	5.5	X		
99:03:25	08:33:27	39.596	77.235	57	5.1	X		
99:03:28	19:05:11	30.512	79.403	15	6.4	X	X	
99:03:28	21:33:44	85.644	86.259	10	5.0	X		
99:03:29	01:27:09	14.433	-88.399	33	5.1	X		
99:03:30	09:59:07	10.696	-70.418	10	5.6	X		
99:03:31	05:54:42	5.827	-82.616	10	5.9	X	X	
99:03:31	12:45:36	85.624	86.568	10	4.8	X		
99:03:31	23:18:03	-8.975	-109.474	10	5.0	X		
99:04:01	10:47:53	85.648	86.531	10	5.1	X		
99:04:01	21:36:21	-4.357	152.707	33	5.6	X	X	

Table A.1: (Continued)

Date YY:MM:DD	Time hh:mm:ss.s	Latitude °N	Longitude °E	Depth km	m_b	TTI-*P*	RF	SWS
99:04:04	10:37:00	16.097	-97.341	33	5.1	X		
99:04:06	00:08:22	39.400	38.307	10	5.1	X		
99:04:06	04:51:05	24.451	-46.374	10	5.3	X		
99:04:08	13:10:34	43.607	130.350	566	6.4	X	X	
99:04:09	12:16:01	-26.354	178.221	621	5.5	X	X	
99:04:11	19:15:18	18.452	145.154	513	4.5	X		
99:04:12	01:54:16	-22.864	-70.466	40	4.9	X		
99:04:13	10:38:48	-21.422	-176.460	164	6.4	X	X	X
99:04:14	07:25:04	6.772	-72.946	161	4.8	X		
99:04:17	00:56:25	19.248	-155.489	11	5.6	X	X	
99:04:17	07:20:55	38.213	75.518	137	4.9	X		
99:04:17	08:17:58	36.038	21.683	40	4.7	X		
99:04:18	23:14:19	34.192	139.460	129	4.8	X		
99:04:19	09:12:47	50.888	156.423	118	5.4	X		
99:04:20	01:46:17	-18.791	-177.957	586	5.1	X		
99:04:20	19:04:08	-31.888	-179.040	96	6.2	X		X
99:04:23	18:56:26	13.123	145.142	53	5.5	X	X	
99:04:24	08:45:16	-18.043	-178.449	568	5.2	X		
99:04:25	09:10:44	-31.798	-69.255	116	5.3	X		
99:04:25	12:27:05	36.441	140.473	82	5.3	X		
99:04:26	07:07:02	53.965	159.190	127	4.8	X		
99:04:26	13:20:07	85.672	84.830	10	5.2	X		
99:04:26	18:17:26	-1.648	-77.783	173	5.6	X	X	
99:04:28	08:47:55	45.464	26.183	156	5.1	X		
99:04:28	08:47:55	45.464	26.183	156	5.1	X		
99:04:29	07:46:08	28.867	131.148	33	5.8	X	X	
99:04:29	15:01:18	-26.611	-114.396	10	5.1	X		
99:04:30	03:30:38	44.181	20.071	14	5.0	X		
99:05:02	16:13:50	56.794	-34.268	10	5.3	X		
99:05:02	20:39:26	29.083	131.212	33	5.1	X		
99:05:05	22:41:30	14.364	-94.673	33	5.8	X	X	
99:05:08	05:11:54	11.509	-86.793	62	4.9	X		
99:05:08	19:44:35	45.449	151.630	63	6.2	X	X	
99:05:08	22:12:45	14.214	-91.945	39	5.3	X		
99:05:10	08:47:25	-30.397	-69.163	65	5.2	X		
99:05:10	20:33:02	-5.159	150.880	138	6.5	X	X	X
99:05:12	17:59:22	43.032	143.835	103	5.9	X	X	

Table A.1: (Continued)

Date YY:MM:DD	Time hh:mm:ss.s	Latitude °N	Longitude °E	Depth km	m_b	TTI-*P*	RF	SWS
99:05:16	00:51:20	-4.751	152.486	74	6.0	X	X	
99:05:16	15:25:53	-2.642	138.217	59	6.1	X		
99:05:17	10:07:56	-5.165	152.877	27	5.5		X	
99:05:18	20:20:16	85.632	86.146	10	5.1	X		
99:05:19	18:40:00	15.896	-92.929	95	4.7	X		
99:05:21	04:31:25	-22.886	-68.520	130	4.7	X		
99:05:25	16:42:05	-27.931	-66.934	169	5.3	X		
99:05:26	23:56:32	85.605	86.526	10	5.1	X		
99:05:28	04:52:55	12.568	-87.377	86	5.3	X		
99:05:30	15:56:45	55.796	110.030	10	5.3	X		
99:06:02	07:34:41	-20.858	-179.002	644	5.0	X		
99:06:07	16:10:33	73.017	5.187	10	5.3	X		
99:06:07	16:35:46	73.077	5.453	10	5.2	X		
99:06:08	12:04:00	15.040	-60.421	55	5.3	X		
99:06:09	00:02:04	-19.281	-173.557	33	5.0	X		
99:06:09	07:07:31	49.316	158.396	33	5.2	X		
99:06:10	09:08:13	56.137	-161.609	172	4.7	X		
99:06:10	15:07:21	36.237	71.212	112	5.2	X		
99:06:11	07:50:15	37.560	21.110	58	4.8	X		
99:06:13	22:48:21	13.872	-50.152	10	5.0	X		
99:06:15	20:42:05	18.386	-97.436	70	6.4	X	X	
99:06:16	18:35:59	-17.037	-173.362	75	5.6		X	
99:06:21	17:43:04	18.324	-101.539	69	6.0	X	X	
99:06:26	22:05:28	-17.956	-178.187	590	5.3	X		
99:06:29	05:50:89	-9.468	147.854	33	5.8		X	
99:06:29	10:55:11	-15.710	-72.496	118	5.1	X		
99:06:29	23:18:05	36.622	71.353	189	5.9	X	X	
00:04:23	09:27:22	-28.250	-62.890	603	6.9			X
00:04:23	17:01:17	-28.280	-62.820	610	6.1			X

Appendix B

Scattering potentials

This appendix gives the full expressions for the scattering potentials,

$$f^q(\mathbf{x},\theta) = \sum_{l=1}^{3} W_l^q(\theta)\Delta m_l(\mathbf{x}), \tag{B.1}$$

which include the θ-dependent radiation patterns $W_l^q(\theta)$ and material property perturbations $\Delta m_l(\mathbf{x})$=$(\Delta\alpha/\alpha, \Delta\beta/\beta, \Delta\rho/\rho)$. These expressions are derived in *Paper I* for different scattering modes:

$$f^{1,3}(\mathbf{x},\theta) = \rho^0 \left(2\frac{\Delta\alpha}{\alpha^0} + \frac{\Delta\beta}{\beta^0}\left(2\left(\frac{\beta^0}{\alpha^0}\right)^2(\cos 2\theta - 1)\right) + \frac{\Delta\rho}{\rho^0}\left(1 + \cos\theta + \left(\frac{\beta^0}{\alpha^0}\right)^2(\cos 2\theta - 1)\right)\right), \tag{B.2}$$

$$f^{2,4}(\mathbf{x},\theta) = \rho^0 \left(\frac{\Delta\beta}{\beta^0}\left(2\frac{\beta^0}{\alpha^0}\sin 2\theta\right) + \frac{\Delta\rho}{\rho^0}\left(\sin\theta + \frac{\beta^0}{\alpha^0}\sin 2\theta\right)\right), \tag{B.3}$$

$$f^{5}(\mathbf{x},\theta) = \rho^0 \left(\frac{\Delta\beta}{\beta^0}\left(2\frac{\beta^0}{\alpha^0}\sin 2\theta\right) + \frac{\Delta\rho}{\rho^0}\left(\sin\theta + \frac{\beta^0}{\alpha^0}\sin 2\theta\right)\right), \tag{B.4}$$

$$f^{6}(\mathbf{x},\theta) = \rho^0 \left(\frac{\Delta\beta}{\beta^0}(2\cos 2\theta) + \frac{\Delta\rho}{\rho^0}(\cos\theta + \cos 2\theta)\right), \tag{B.5}$$

$$f^{7}(\mathbf{x},\theta) = \rho^0 \left(\frac{\Delta\beta}{\beta^0}(2\cos\theta) + \frac{\Delta\rho}{\rho^0}(1 + \cos\theta)\right). \tag{B.6}$$